Check for updates

ADVANCING EARTH AND SPACE SCIENCES

JAMES | Journal of Advances in Modeling Earth Systems®

RESEARCH ARTICLE
10.1029/2025MS005643

Crowdsourcing the Frontier: Advancing Hybrid Physics-ML Climate Simulation via a $50,000 Kaggle Competition

Jerry Lin[1,2], Zeyuan Hu[3], Tom Beucler[4,5], Katherine Frields[1], Hannah Christensen[6], Walter Hannah[7], Helge Heuer[8], Peter Ukkonen[6], Laura A. Mansfield[6], Tian Zheng[9], Liran Peng[1], Ritwik Gupta[10,11], Pierre Gentine[12], Yusef Al-Naher[13], Mingjiang Duan[14], Kyo Hattori[15], Weiliang Ji[14], Chunhan Li[14], Kippei Matsuda[16], Naoki Murakami[17], Shlomo Ron[18], Marec Serlin[19], Hongjian Song[14], Yuma Tanabe[20], Daisuke Yamamoto[21], Jianyao Zhou[22], and Mike Pritchard[1,3]

[1]Department of Earth System Sciences, University of California at Irvine, Irvine, CA, USA, [2]Department of Computing & Data Sciences, Boston University, Boston, MA, USA, [3]NVIDIA Research, Santa Clara, CA, USA, [4]Faculty of Geosciences and Environment, University of Lausanne, Lausanne, Switzerland, [5]Expertise Center for Climate Extremes, University of Lausanne, Lausanne, Switzerland, [6]Department of Physics, University of Oxford, Oxford, UK, [7]Lawrence Livermore National Laboratory, Livermore, CA, USA, [8]Deutsches Zentrum für Luft- und Raumfahrt, Institut für Physik der Atmosphäre, Wessling, Germany, [9]Department of Statistics, Columbia University, New York, NY, USA, [10]University of California, Berkeley, Berkeley, CA, USA, [11]University of Maryland, College Park, MD, USA, [12]LEAP Science and Technology Center, School of Engineering and Applied Sciences, Climate School, Columbia University, New York, NY, USA, [13]Unaffiliated, Amsterdam, The Netherlands, [14]Z Lab, Hangzhou, China, [15]ABEJA Inc., Nagoya, Japan, [16]Kawasaki Heavy Industries, Ltd., Kobe, Japan, [17]DeNA Co., Ltd, Tokyo, Japan, [18]Unaffiliated, Ramat Gan, Israel, [19]Uber Technologies, Inc., Seattle, WA, USA, [20]Unaffiliated, Kyoto, Japan, [21]Unaffiliated, Nara, Japan, [22]Unaffiliated, Melbourne, VIC, Australia

Key Points:

- Online stability in the low-resolution real-geography setting is reproducibly achievable across diverse architectures
- Offline and online zonal mean biases are near-identical across architectures; online runs underestimate tropical precipitable water
- An expanded variable list is universally beneficial offline but has diverging, architecture-dependent effects online

Supporting Information:

Supporting Information may be found in the online version of this article.

Correspondence to:

J. Lin,
jlin404@bu.edu

Citation:

Lin, J., Hu, Z., Beucler, T., Frields, K., Christensen, H., Hannah, W., et al. (2026). Crowdsourcing the frontier: Advancing hybrid physics-ML climate simulation via a $50,000 Kaggle competition. *Journal of Advances in Modeling Earth Systems*, *18*, e2025MS005643. https://doi.org/10.1029/2025MS005643

Received 25 NOV 2025
Accepted 13 APR 2026

Author Contributions:

Conceptualization: Jerry Lin, Yusef Al-Naher, Kyo Hattori, Weiliang Ji, Chunhan Li, Kippei Matsuda, Naoki Murakami, Shlomo Ron, Marec Serlin, Hongjian Song, Yuma Tanabe, Daisuke Yamamoto, Jianyao Zhou, Mike Pritchard
Formal analysis: Jerry Lin, Zeyuan Hu, Tom Beucler
Funding acquisition: Pierre Gentine, Mike Pritchard
Investigation: Jerry Lin
Methodology: Jerry Lin, Hannah Christensen, Walter Hannah, Liran Peng, Ritwik Gupta, Mike Pritchard

© 2026 The Author(s). Journal of Advances in Modeling Earth Systems published by Wiley Periodicals LLC on behalf of American Geophysical Union. This is an open access article under the terms of the Creative Commons Attribution License, which permits use, distribution and reproduction in any medium, provided the original work is properly cited.

Abstract Subgrid machine-learning (machine learning [ML]) parameterizations have the potential to introduce a new generation of climate models that incorporate the effects of higher-resolution physics without incurring the prohibitive computational cost associated with more explicit physics-based simulations. However, important issues, ranging from online instability to inconsistent online performance, have limited their operational use for long-term climate projections. To more rapidly drive progress in solving these issues, domain scientists and ML researchers opened up the offline aspect of this problem to the broader ML and data science community with the release of ClimSim, a NeurIPS Data sets and Benchmarks publication, and an associated Kaggle competition. This paper reports on the downstream results of the Kaggle competition by coupling emulators inspired by the winning teams' architectures to an interactive climate model (including full cloud microphysics, a regime historically prone to online instability) and systematically evaluating their online performance. Our results demonstrate that online stability in the low-resolution real-geography setting is reproducible across multiple diverse architectures, which we consider a key milestone. All tested architectures exhibit strikingly similar offline and online biases, though their responses to architecture-agnostic design choices (e.g., expanding the list of input variables) can differ significantly. Multiple Kaggle-inspired architectures achieve state-of-the-art results on certain metrics such as zonal mean bias patterns and global Root Mean Squared Error, indicating that crowdsourcing the essence of the offline problem is one path to improving online performance in hybrid physics-AI climate simulation.

Plain Language Summary Future climate models may use machine learning (ML) to replace small-scale physical processes that are otherwise too costly to simulate directly over long timescales. Such "hybrid" physics–ML models could improve predictions by reducing uncertainties from current approximations. But making them run reliably in full climate simulations has been a major challenge. To speed progress, scientists created an open data set, benchmarking framework, and global competition to drive improvement for these ML components. This paper follows up on that competition by testing ideas from the winning teams within hybrid climate models. For the first time, we show that stable hybrid simulation is now reproducible across a range of diverse ML architectures. We find that different architectures share similar patterns of errors both before and after coupling, although their responses to added training inputs can differ. Finally, some competition-inspired designs achieve state-of-the-art scores on individual performance measures, but no single approach beats the previous benchmark (Hu et al., 2025, https://doi.org/10.1029/2024ms004618) on every metric.

Project administration: Tian Zheng, Ritwik Gupta, Pierre Gentine, Mike Pritchard
Software: Jerry Lin, Zeyuan Hu, Katherine Frields, Yusef Al-Naher, Kyo Hattori, Weiliang Ji, Chunhan Li, Kippei Matsuda, Naoki Murakami, Shlomo Ron, Marec Serlin, Hongjian Song, Yuma Tanabe, Daisuke Yamamoto, Jianyao Zhou
Supervision: Tom Beucler, Walter Hannah, Tian Zheng, Pierre Gentine, Mike Pritchard
Validation: Jerry Lin, Zeyuan Hu
Visualization: Jerry Lin
Writing – original draft: Jerry Lin
Writing – review & editing: Jerry Lin, Zeyuan Hu, Tom Beucler, Hannah Christensen, Walter Hannah, Mike Pritchard

1. Introduction

Earth system models (or simpler climate models) used for contemporary long-term projections operate at a coarse resolution (> 25 km along the horizontal) and rely on hand-tuned subgrid parameterizations that imperfectly represent the effects of subgrid processes like convection, radiation, and turbulence, resulting in systematic biases and large error bars in the amount of expected warming (Ceppi & Hartmann, 2016; O'Gorman, 2012; Schneider et al., 2017; Sherwood et al., 2014; Webb et al., 2013). To improve the representation of deep convection and clouds, the climate modeling community is actively exploring the use of computationally expensive kilometer-scale global simulations (Hohenegger et al., 2023; Taylor et al., 2023). However, even at these resolutions, convection is only partially resolved and the need for parameterizations for processes like turbulence or microphysics is never fully eliminated (Schneider et al., 2017; Taylor et al., 2023). In addition, this approach becomes intractable when considering the fact that multiple realizations of future climates over long time horizons and emissions scenarios are required for proper uncertainty quantification, depiction of extremes, and actionable adaptation (Kay et al., 2015).

An alternative approach for more explicitly resolving some subgrid processes without relying on a natively high-resolution discretization is Multiscale Modeling Framework (MMF), also known as superparameterization (Khairoutdinov et al., 2005; Randall, 2013; Randall et al., 2003). In MMF, a Cloud Resolving Model (CRM) with periodic boundary conditions and higher spatial and temporal resolution than the host climate model is embedded inside each coarse-model grid cell. The effective kilometer scale resolution in the MMF approach yields several tangible benefits, ranging from improvements in the representation of precipitation extremes to more faithfully reproducing the periodicity of the El Niño Southern Oscillation (Li et al., 2012; Randall, 2013; Stan et al., 2010). Ultimately, this approach has not been adopted for long-term climate projections as the computational cost remains prohibitively high (Gentine et al., 2018). Additionally, the artificial scale separation that allows for massively parallel computation in MMF introduces unnatural artifacts and its own set of compromises for the sake of computational efficiency (Jansson et al., 2022; W. Hannah & Pressel, 2022). Because of this and other factors, more effort has been devoted to advancing Global Cloud Resolving Models (GCRMs) for operational use in recent years.

Interestingly, the clean spatial and temporal scale separation between the embedded CRMs and GCM in the MMF approach has conveniently (albeit unintentionally) given birth to a new means for bringing kilometer scale fidelity at a fraction of the computational cost. This is because the MMF approach integrates CRMs within the GCM framework at the GCM's native spatial and temporal resolution. This process inherently summarizes ("coarse-grains") the CRM behavior to the GCM scale at each timestep, making the CRM output a natural target for emulation by machine learning (ML) models, particularly neural networks (NNs) (Gentine et al., 2018; Han et al., 2023; Mooers et al., 2021; Rasp et al., 2018). Unfortunately, this promise remains unrealized despite years of interest because of emergent failure modes when deploying these ML models in an "online" setting (i.e., when dynamically coupled to the GCM) (Brenowitz et al., 2020; Chen et al., 2025; Lin et al., 2025). Online emulation has proved particularly challenging in the limit of full complexity emulation of the CRMs used in MMFs, such as when difficult-to-emulate microphysical tendencies are included in the scale coupling. To engage the machine learning (ML) research community on these issues, a group of climate scientists and ML researchers released ClimSim, a NeurIPS Data sets and Benchmarks publication, software repository, and collection of data sets consisting of multivariate CRM input-output pairs generated using the Energy Exascale Earth System Model-Multiscale Modeling Framework (E3SM-MMF) (See Section 2.1 in Methods for more details) (Yu et al., 2023). This was followed up by Hu et al. (2025), which showcased stable 5-year online simulations with explicit cloud condensate coupling for the first time, and ClimSim-Online, which democratized online testing via a containerized version of E3SM-MMF (Yu et al., 2025). In parallel, the official ClimSim Kaggle competition ran for three months during the summer of 2024, attracting approximately 700 teams from around the world who submitted over 10,000 predictions in pursuit of a $50,000 prize pool (Lin et al., 2024).

Our hypothesis is that by expanding both awareness and accessibility of this research problem to those in the data science and ML community, we can facilitate advancements that would not have happened had this research problem stayed confined to domain scientists limited by time, personnel, and funding constraints. Thanks to the visibility of Kaggle, which is widely considered the leading platform for data science and ML competitions, the CRM emulation problem attracted the talents of some of the world's best data scientists and ML engineers in a short timeframe. The leaderboard revealed that hundreds of teams were able to surpass the strongest offline R^2

19422466, 2026, 5, Downloaded from https://agupubs.onlinelibrary.wiley.com/doi/10.1029/2025MS005643 by Dtsch Zentrum F. Luft-U. Raum Fahrt In D. Helmholtz Gemein., Wiley Online Library on [27/10/2026]. See the Terms and Conditions (https://onlinelibrary.wiley.com/terms-and-conditions) on Wiley Online Library for rules of use; OA articles are governed by the applicable Creative Commons License

baseline set using the U-Net architecture from Hu et al., 2025, raising the question—do the same innovations that led to improvements in offline skill also yield benefits online?

This study approaches this question systematically, evaluating both architecture-specific and architecture-agnostic design decisions inspired by the top of the Kaggle leaderboard online. The following results will demonstrate their methods' potential to achieve state-of-the-art hybrid simulation results and will reveal aspects of the hybrid physics-ML simulation problem that remain resistant to Kaggle-inspired innovations. In the low-resolution real-geography ClimSim limit, we can report that online stability when including the complexity of full microphysical coupling is reproducibly achievable across diverse architectures going forward. However, different architectures can respond differently to architecture-agnostic design decisions in ways that can cause one architecture to experience less online drift and another to become completely unstable online. This is particularly evident when expanding the input variable list to include convective memory, large-scale forcings, and latitudinal information. Nevertheless, both offline and online biases are structurally similar across all architectures and architecture-agnostic design decisions, and offline biases across multiple variables change systematically as a function of precipitation percentile. In the following sections, we showcase how Kaggle-inspired innovations have pushed the frontier of hybrid physics-ML climate simulation while isolating the remaining challenges that lie ahead.

2. Methods

Designing a reasonably controlled and scientific intercomparison inspired by top Kaggle users' decisions naturally required several trade-offs. In order to make our post-competition analysis tractable, we do not exhaustively investigate every architecture and architecture-agnostic design decision utilized in the winning solutions from the Kaggle competition. This would be impractical as winning solutions were often composed of a weighted average of vastly different architectures highly optimized for strong performance on a singular offline scalar metric (averaged R^2 across all target variables). Instead, we intercompare online performance of five architectures inspired by the methods of the five winning teams alongside the U-Net architecture of Hu et al. (2025), a strong baseline. We evaluate both offline and online performance using held-out simulation data from MMF as ground truth (see Section 2.1 for details). Additional details regarding calculation of R^2, Root Mean Squared Error (RMSE), and zonal averaging can be found in Texts S1–S3 in Supporting Information S1. With the exception of architectures in the multirepresentation configuration, which uses multiple variations of the input using different input normalizations (detailed in Section 2.3.4), all models use the same input normalizations, output normalizations, microphysics constraint, and feature pruning used in Hu et al. (2025). Details regarding input and output normalizations as well as feature pruning are detailed in Tables 1–3. The microphysics constraint, as seen in Figure 2 from Hu et al. (2025), mirrors the one-moment microphysics scheme in the CRM, using temperature to diagnose the mixing ratio of liquid and ice cloud. While the diagnostic relationship does not hold exactly on the GCM grid scale, the constraint was shown to greatly reduce online biases in Hu et al. (2025). Each architecture is trained across five configurations using architecture-agnostic design decisions inspired by the Kaggle competition winners as well as the input variable list expansion developed by Hu et al. (2025). We make no modifications to the hyperparameters when adapting architectures from the winning solutions in the Kaggle competition. To gauge variability induced by choice of seed, we train three models for each architecture and configuration pair using different seeds. This yields a total of 90 models that we trained for the entire study (6 architectures × 5 configurations × 3 seeds). All models were coupled online to the same MMF used to generate the ClimSim data, using an FTorch binding to facilitate GPU-accelerated hybrid simulations (Atkinson et al., 2025).

For our Kaggle architectures, we chose the *Squeezeformer* from the first place team, the *Pure ResLSTM* from the second place team, a custom architecture called the *Pao Model* from the third place team, a *ConvNeXt* convolutional NN from the fourth place team, and an *Encoder-Decoder Long Short-Term Memory (LSTM)* from the fifth place team. Feature selection, preprocessing, postprocessing, and training settings such as batch size, number of epochs, loss function, learning rate, and learning rate scheduler were unified across all architectures to facilitate fairer comparisons. To understand how different architectures responded to different architecture-agnostic design decisions, we created "standard," "confidence loss," "difference loss," "multirepresentation," and "expanded variable list" configurations (detailed in Section 2.2). Input variables and input normalizations for the "standard," "confidence loss," and "difference loss" configurations are the same and are shown in Table 1. The "multirepresentation" configuration makes use of the same input variables but across three separate normalizations. The

19422466, 2026, 5, Downloaded from https://agupubs.onlinelibrary.wiley.com/doi/10.1029/2025MS005643 by Dtsch Zentrum F. Luft-U. Raum Fahrt In D. Helmholtz Gemein., Wiley Online Library on [27/10/2026]. See the Terms and Conditions (https://onlinelibrary.wiley.com/terms-and-conditions) on Wiley Online Library for rules of use; OA articles are governed by the applicable Creative Commons License

Table 1
List of Input Features Used in the Standard, Confidence Loss, and Difference Loss Configurations

Variable	Units	Description	Normalization
$T(z)$	K	Temperature	(x-mean)/(max-min)
$RH(z)$		Relative humidity	
$q_n(z)$	kg/kg	Liquid and ice cloud mixing ratio	$1 - \exp(-\lambda x)$
Liquid partition (z)		Diagnostic microphysics constraint	
$u(z)$	m/s	Zonal wind	(x-mean)/(max-min)
$v(z)$	m/s	Meridional wind	(x-mean)/(max-min)
O3(z)	mol/mol	Ozone volume mixing ratio	(x-mean)/(max-min)
CH4(z)	mol/mol	Methane volume mixing ratio	(x-mean)/(max-min)
N2O(z)	mol/mol	Nitrous volume mixing ratio	(x-mean)/(max-min)
PS	Pa	Surface pressure	(x-mean)/(max-min)
SOLIN	W/m^2	Solar insolation	x/(max-min)
LHFLX	W/m^2	Surface latent heat flux	x/(max-min)
SHFLX	W/m^2	Surface sensible heat flux	x/(max-min)
TAUX	W/m^2	Zonal surface stress	(x-mean)/(max-min)
TAUY	W/m^2	Meridional surface stress	(x-mean)/(max-min)
COSZRS		Cosine of solar zenith angle	(x-mean)/(max-min)
ALDIF		Albedo for diffuse longwave radiation	(x-mean)/(max-min)
ALDIR		Albedo for direct longwave radiation	(x-mean)/(max-min)
ASDIF		Albedo for diffuse shortwave radiation	(x-mean)/(max-min)
ASDIR		Albedo for direct shortwave radiation	(x-mean)/(max-min)
LWUP	W/m^2	Surface upward longwave flux	(x-mean)/(max-min)
ICEFRAC		Sea-ice area fraction	
LANDFRAC		Land area fraction	
OCNFRAC		Ocean area fraction	
SNOWHICE	m	Snow depth over ice	(x-mean)/(max-min)
SNOWHLAND	m	Snow depth over land	(x-mean)/(max-min)

Note. Here $\lambda = 1/\overline{q_n^*}$, where $\overline{q_n^*}$ refers to the average liquid and ice cloud mixing ratio for liquid and ice cloud mixing ratios $> 10^{-7}$.

"expanded variable list" configuration incorporates additional input variables (shown in Table 3) that matches what was used for the U-Net-expanded model seen in Hu et al. (2025). All models across all configurations share the same output variables and output normalizations, which are listed in Table 2.

2.1. Data Set and Reference Climate Simulation

ClimSim provides three different 10-year simulations generated by E3SM-MMF of varying complexity: a low-resolution aquaplanet version, a low-resolution real-geography version, and a high-resolution real-geography version. All NNs in this study were trained, validated, and tested (offline) using the low-resolution real-geography version. This version was configured using the "F2010-MMF1" compset and "ne4pg2" grid (Yu et al., 2025). The effective horizontal resolution for the GCM is extremely coarse at approximately 11.5° × 11.5° as there are only 384 columns arranged in an unstructured, cubed-sphere grid. Each GCM column is composed of 60 vertical levels extending up to 65 km in altitude, and the model timestep is 20 min. The embedded CRMs are 2D and aligned in the north-south direction with 64 columns across their domain and 2 km horizontal grid spacing. The forcing from the GCM on the domain mean of each CRM is 1D, and the CRMs are not designed to have spatial information that correspond to actual locations on the globe. Taking advantage of the clean scale separation provided by MMF, only data at the GCM grid's discretization is used for training, validation, and testing. Sea Surface Temperatures

19422466, 2026, 5, Downloaded from https://agupubs.onlinelibrary.wiley.com/doi/10.1029/2025MS005643 by Dtsch Zentrum F. Luft-U. Raum Fahrt In D. Helmholtz Gemein., Wiley Online Library on [27/10/2026]. See the Terms and Conditions (https://onlinelibrary.wiley.com/terms-and-conditions) on Wiley Online Library for rules of use; OA articles are governed by the applicable Creative Commons License

Table 2
List of Output Variables Used by All Models

Variable	Units	Description	Normalization
$dT/dt(z,t_0)$	K/s	Temperature tendency	x/std
$dq_v/dt(z,t_0)$	kg/kg/s	Water vapor tendency	x/min (std,γ_1)
$dq_n/dt(z,t_0)$	kg/kg/s	Liquid and ice cloud tendency	x/min (std,γ_1)
$du/dt(z,t_0)$	m/s^2	Zonal wind tendency	x/min (std,γ_2)
$dv/dt(z,t_0)$	m/s^2	Meridional wind tendency	x/min (std,γ_2)
NETSW	W/m^2	Net shortwave flux at surface	x/std
FLWDS	W/m^2	Downward longwave flux at surface	x/std
PRECSC	m/s	Snow rate (liquid water equivalent)	x/std
PRECC	m/s	Rain rate	x/std
SOLS	W/m^2	Downward visible direct solar flux to surface	x/std
SOLL	W/m^2	Downward near-IR direct solar flux to surface	x/std
SOLSD	W/m^2	Downward visible diffuse solar flux to surface	x/std
SOLLD	W/m^2	Downward near-IR diffuse solar flux to surface	x/std

Note. γ_1 and γ_2 are lower bounds to prevent the output normalizations from creating value that are too large. $\gamma_1 = 3^{-10}$ and $\gamma_2 = 10^{-6}$. The top 15 levels of neural network output tendencies for water vapor, total cloud, and both zonal and meridional wind are "pruned" and set to 0.

(SSTs) and sea ice coverage are prescribed to be similar to present-day climatology (with SSTs varying according to a fixed annual cycle), and aerosols are transparent to radiation code. The first 7 years and 1st month of the 8th year of the simulation data are used for training, the rest of the 8th year and the first month of the 9th year are used for validation, and rest of the final 2 years are used for offline testing. No subsampling was used to create the training data set, but the validation data set subsamples every seventh timestep while the test data set subsamples every 12th timestep. This yields 69,783,552 samples for the training data (235.2 GB), 1,564,086 samples for the validation data (4.7 GB), and 1,681,920 samples for the test data (5.5 GB). The storage sizes shown here are after preprocessing using the "standard" variable list, described in Section 2.3.1 and shown in Tables 1 and 2.

Table 3
List of Additional Input Features Used in the Expanded Variable List Configuration

Variable	Units	Description	Normalization
$dT_{adv}/dt(z,t_0)$	K/s	Large-scale forcing of temperature at (t)	x/(max-min)
$dq_{T,adv}/dt(z,t_0)$	kg/kg/s	Large-scale forcing of total water at (t)	x/(max-min)
$du_{adv}/dt(z,t_0)$	m/s^2	Large-scale forcing of zonal wind at (t)	x/(max-min)
$dT_{adv}/dt(z,t_{-1})$	K/s	Large-scale forcing of temperature at ($t-1$)	x/(max-min)
$dq_{T,adv}/dt(z,t_{-1})$	kg/kg/s	Large-scale forcing of total water at ($t-1$)	x/(max-min)
$du_{adv}/dt(z,t_{-1})$	m/s^2	Large-scale forcing of zonal wind at ($t-1$)	x/(max-min)
$dT/dt(z,t_{-1})$	K/s	Temperature tendency at ($t-1$)	x/std
$dq_v/dt(z,t_{-1})$	kg/kg/s	Water vapor tendency at ($t-1$)	x/std
$dq_n/dt(z,t_{-1})$	kg/kg/s	Total cloud tendency at ($t-1$)	x/std
$du/dt(z,t_{-1})$	m/s^2	Zonal wind tendency at ($t-1$)	x/std
$dT/dt(z,t_{-2})$	K/s	Temperature tendency at ($t-2$)	x/std
$dq_v/dt(z,t_{-2})$	kg/kg/s	Water vapor tendency at ($t-2$)	x/std
$dq_n/dt(z,t_{-2})$	kg/kg/s	Total cloud tendency at ($t-2$)	x/std
$du/dt(z,t_{-2})$	m/s^2	Zonal wind tendency at ($t-2$)	x/std
cos(lat)		Cosine of latitude	
sin(lat)		Sine of latitude	

19422466, 2026, 5, Downloaded from https://agupubs.onlinelibrary.wiley.com/doi/10.1029/2025MS005643 by Dtsch Zentrum F. Luft-U. Raum Fahrt In D. Helmholtz Gemein., Wiley Online Library on [27/10/2026]. See the Terms and Conditions (https://onlinelibrary.wiley.com/terms-and-conditions) on Wiley Online Library for rules of use; OA articles are governed by the applicable Creative Commons License

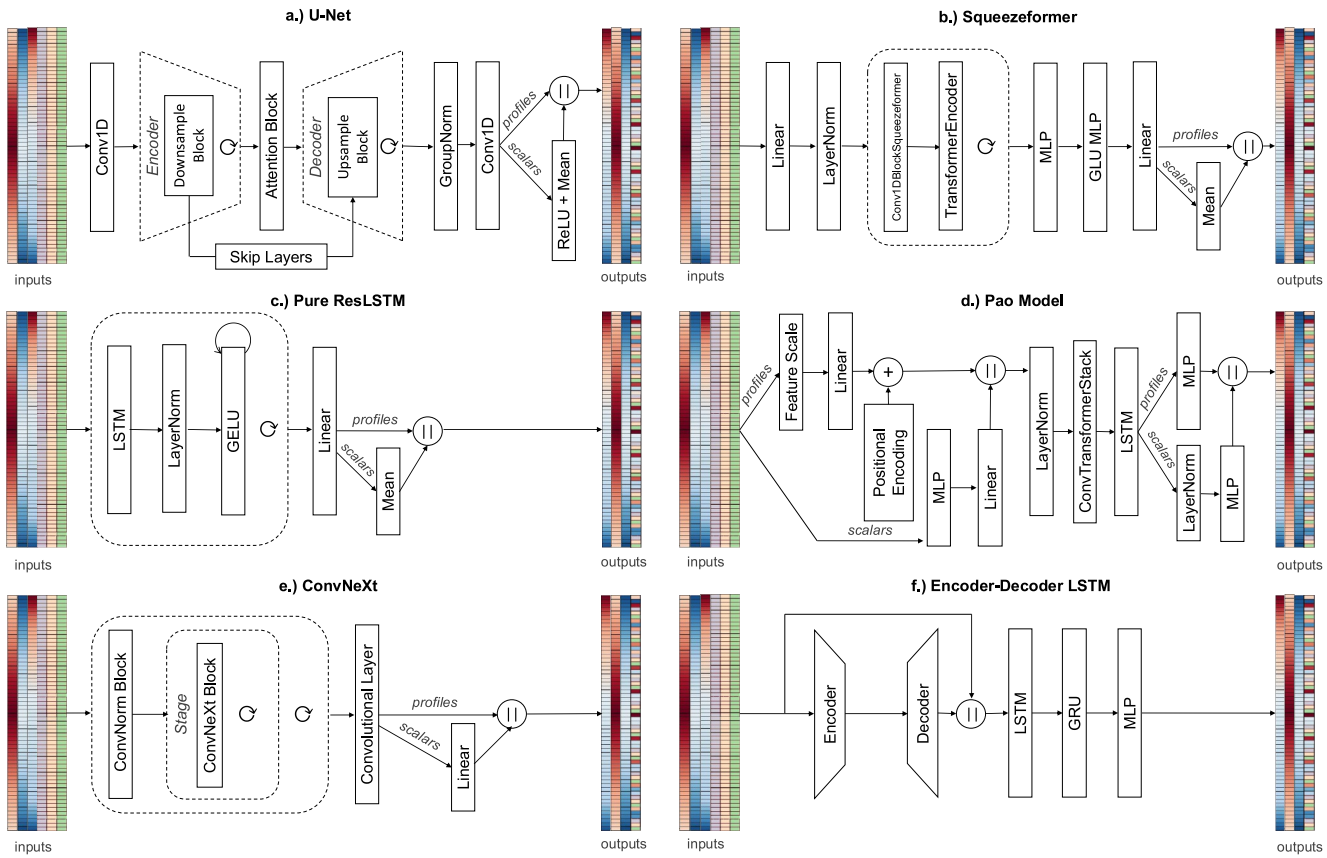

Figure 1. Architecture diagrams for the U-Net from (Hu et al., 2025), Squeezeformer, Pure ResLSTM, Pao Model, ConvNeXt, and Encoder-Decoder Long Short-Term Memory from the first place, second place, third place, fourth place, and fifth place teams in the 2024 LEAP ClimSim Kaggle competition.

For online simulation and testing, both hybrid runs and the MMF reference run used a different initial condition than that used to create the original ClimSim data set. This was necessary because the original data set did not provide restart files, requiring us to start from a spun-up state rather than from scratch.

Since our NN parameterizations are trained exclusively on a low-resolution MMF simulation, and our primary goal is to advance fundamental hybrid modeling challenges—such as stability, reliability, and both offline and online accuracy relative to MMF—we omit direct comparisons of our hybrid simulations to ERA5 reanalysis or observations. For similar reasons, we also refrain from comparing against E3SM configurations that use traditional parameterizations (e.g., E3SMv1, E3SMv2, and E3SMv3). These non-MMF versions are fundamentally different models that were not tuned to reproduce E3SM-MMF behavior. Moreover, prior studies have already compared E3SM-MMF to its non-MMF counterparts, in some cases identifying biases or unphysical artifacts unique to E3SM-MMF (W. M. Hannah et al., 2020, 2025; Xia et al., 2025).

2.2. Architectures

2.2.1. U-Net Baseline

The U-Net architecture is taken from Hu et al. (2025), which itself was adapted from a 2-D U-Net created for score-based diffusion modeling in Song et al. (2020). In this architecture, shown in Figure 1a, an encoder progressively downsamples the vertical dimension while expanding the feature space (i.e., channels), and the decoder reverses this operation. Skip connections directly link layers of the encoder to corresponding layers of the decoder, preserving fine-grained details that might be lost during the downsampling process. The scalar output variables, which are each represented by a channel of 60 values, are made non-negative via a ReLU function and condensed into scalar values (i.e., $\mathbb{R}^{60} \rightarrow \mathbb{R}^{1}$) via averaging. These scalar values are then concatenated back to the

19422466, 2026, 5, Downloaded from https://agupubs.onlinelibrary.wiley.com/doi/10.1029/2025MS005643 by Dtsch Zentrum F. Luft-U. Raum Fahrt In D. Helmholtz Gemein., Wiley Online Library on [27/10/2026]. See the Terms and Conditions (https://onlinelibrary.wiley.com/terms-and-conditions) on Wiley Online Library for rules of use; OA articles are governed by the applicable Creative Commons License

vertically-resolved output variables for the final output vector. This architecture serves as a useful baseline against which to compare winning architectures from the Kaggle competition.

2.2.2. Squeezeformer

The Squeezeformer, shown in Figure 1b, is an architecture used by the first place team in the Kaggle competition. Originally invented for automatic speech recognition by Kim et al. (2022), this architecture has been successful in other contexts, having been used for first and second place finishes in Kaggle competitions for fingerspelling recognition and RNA folding, respectively (Chow et al., 2023; Das et al., 2023). This architecture integrates convolutional and transformer components to process sequential data. Initially, input variables are projected into a high-dimensional embedding space of 384 features by a linear layer, followed by layer normalization. The core of the network consists of a series of identical blocks stacked together. Each block first passes the data through a `Conv1DBlockSqueezeformer` to capture local contextual information as well as relationships between features, and then through a standard `TransformerEncoder` with multi-head self-attention to model global dependencies across the sequence. The `Conv1DBlockSqueezeformer` blocks are characterized by gated linear units for selective feature activation, depthwise convolutions for cross-feature mixing, and efficient channel attention to adaptively recalibrate channel-wise features. The result is then passed through an MLP that expands the feature space to 2,048 dimensions. This is followed by a Gated Linear Unit Multi-Layer Perceptron, which projects the features into a lower-dimensional embedding space, splits them into two halves, applies a non-linear activation to one half, multiplies the two halves element-wise, and then linearly transforms the output back to 2,048 dimensions. Finally, a linear layer maps the features to the desired number of output variables, and scalar output variables are averaged before being concatenated to the vertically-resolved variables in the final output vector.

2.2.3. Pure ResLSTM

The "Pure ResLSTM", shown in Figure 1c is a multi-layer bidirectional LSTM network adapted from one of the architectures used by the second place team. This architecture consists of multiple LSTM layers, each followed by a layer normalization and Gaussian Error Linear Unit (GELU) activation. The model takes input profiles and scalar features, processes them through 10 blocks each composed of a bidirectional LSTM layer, layer normalization layer, and GELU activation applied to a weighted sum of the current layer and the previous layer. The result is passed through a linear layer, and the channels corresponding to scalar variables are averaged before being concatenated back to the vertically-resolved variables in the final output vector. The use of recurrent NNs across the vertical dimension can be thought of as embedding a physical prior of locality (Ukkonen & Chantry, 2025).

2.2.4. Pao Model

The "Pao Model", shown in Figure 1d, is adapted from an architecture created from scratch by the third place team in the Kaggle competition. This architecture employs a unique strategy for processing vertically-resolved variables and scalar variables separately before and after using a combined representation that is passed through convolutional, transformer, and LSTM elements. Vertically-resolved variables are first linearly scaled and projected into a high-dimensional embedding space of 160 features before being added to a positional embedding that encodes the vertical discretization. Scalar variables are nonlinearly mapped to a 160 dimensional embedding space via an MLP and linear layer. The transformed tensors are then concatenated and fed into a core sequence of residual blocks (composed of convolutional and transformer encoder elements) followed by a two-layer bidirectional LSTM. Finally, the output is split and processed by separate MLPs to produce vertically-resolved variables and scalar output variables before being concatenated together for the final output vector.

2.2.5. ConvNeXt

The "ConvNeXt" model, shown in Figure 1e, is an architecture used by the fourth place team in the Kaggle competition. It is adapted from work by Z. Liu et al. (2022), who invented this new generation of convolutional NNs to be competitive with vision transformers, which have become increasingly dominant for vision tasks. ConvNeXt inspired architectures have also made their way into modern ocean emulators and deep learning weather prediction models (Bonev et al., 2025; Dheeshjith et al., 2024, 2025; Duncan et al., 2025; Karlbauer

19422466, 2026, 5, Downloaded from https://agupubs.onlinelibrary.wiley.com/doi/10.1029/2025MS005643 by Dtsch Zentrum F. Luft-U. Raum Fahrt In D. Helmholtz Gemein., Wiley Online Library on [27/10/2026]. See the Terms and Conditions (https://onlinelibrary.wiley.com/terms-and-conditions) on Wiley Online Library for rules of use; OA articles are governed by the applicable Creative Commons License

et al., 2024). The 1D ConvNeXt model here employs a stack of "ConvNorm blocks" and "stages", alternating between each four times. Each ConvNorm block is composed of a convolutional layer that expands the number of features and a batch normalization layer. The stages are composed of multiple modified ConvNeXt blocks that are each characterized by depthwise convolutions with large kernel sizes for efficient spatial mixing, batch normalization (as opposed to layer normalization), pointwise linear transformations, and a residual connection. The final stage outputs are processed through a convolutional layer that produces combined profile and scalar predictions, with the tensor corresponding to output scalar variables linearly projected into the desired number of output scalar variables.

2.2.6. Encoder-Decoder Long Short-Term Memory

The "Encoder-Decoder LSTM," shown in Figure 1f, is an architecture used by the fifth place team in the Kaggle competition that has already been adopted in follow-up work (Heuer et al., 2025). This architecture first uses an encoder-decoder MLP structure to learn a combined latent representation of all input variables before recurrent processing. The decoded latent representation, which mixes information across variables and levels, is used to create additional input variables for the bidirectional LSTM layer, breaking the locality prior assumed when using vertically recurrent NNs in other ML parameterizations (Ukkonen & Chantry, 2025). The LSTM output is subsequently input into a bidirectional Gated Recurrent Unit (GRU) layer, which refines the sequence representations with a smaller hidden size. Finally, the GRU output is passed through another MLP to generate the final output vector.

2.3. NN Configurations

In this section, we compare five architecture-agnostic design decisions, referred to as "configurations" for short, that were inspired by design decisions made by winners of the Kaggle competition and the input variable feature expansion in Hu et al. (2025). We evaluated these five configurations across all six architectures to detect potential systematic effects. All NNs were trained for 12 epochs with a batch size of 1,024, learning rate of 0.0001, AdamW optimizer, Huber loss, and a learning rate scheduler with a "step" decay strategy in which the learning rate decreases 95% every 3 epochs.

2.3.1. Standard Configuration

The standard configuration serves as a minimal baseline from which other configurations make changes. It can be viewed as identical to the configuration choices of (Hu et al., 2025) except by restricting the input variable list to variables available to Kaggle participants.

2.3.2. Confidence Loss Configuration

The confidence loss configuration is motivated by the "confidence head" used by the first place team and has also recently been adopted by Heuer et al. (2025) in their development of a "confidence-guided mixing parameterization" for transferring knowledge across atmospheric general circulation models. The confidence head mirrors the final prediction layer of the architecture and is used to predict the loss, L_{pred}, for each output in the original prediction layer. The confidence head's prediction for this loss is denoted $\hat{L}_{\text{pred}}$. The loss function for this configuration applies the Huber loss to the sum of the original loss and the loss for the confidence head prediction, L_{loss}. The combined loss is denoted L_{conf}, and the 50/50 weighting used is justified by the fact that the confidence loss is in loss units. Heuer et al. (2025) also showed that this framework can be used for uncertainty estimation; however, our implementation detached the prediction loss being used by the confidence head, preventing this application.

$$L_{\text{pred}} = \text{Huber}(\hat{y}, y)$$

$$L_{\text{loss}} = \text{Huber}\left(\hat{L}_{\text{pred}}, L_{\text{pred}}\right)$$

$$L_{\text{conf}} = L_{\text{pred}} + L_{\text{loss}}$$

19422466, 2026, 5, Downloaded from https://agupubs.onlinelibrary.wiley.com/doi/10.1029/2025MS005643 by Dtsch Zentrum F. Luft-U. Raum Fahrt In D. Helmholtz Gemein., Wiley Online Library on [27/10/2026]. See the Terms and Conditions (https://onlinelibrary.wiley.com/terms-and-conditions) on Wiley Online Library for rules of use; OA articles are governed by the applicable Creative Commons License

19422466, 2026, 5, Downloaded from https://agupubs.onlinelibrary.wiley.com/doi/10.1029/2025MS005643 by Dtsch Zentrum F. Luft-U. Raum Fahrt In D. Helmholtz Gemein., Wiley Online Library on [27/10/2026]. See the Terms and Conditions (https://onlinelibrary.wiley.com/terms-and-conditions) on Wiley Online Library for rules of use; OA articles are governed by the applicable Creative Commons License

2.3.3. Difference Loss Configuration

The difference loss configuration, inspired by the second place team and also adopted by (Heuer et al., 2025), is intended to improve the vertical structure of the predicted tendencies and adds an additional term in the loss function that compares vertical differences for the vertically-resolved variables y_{diff}. The combined loss is denoted L_{total}.

$$L_{\text{pred}} = \text{Huber}(\hat{y}, y)$$

$$L_{\text{diff}} = \text{Huber}\left(\hat{y}_{\text{diff}}, y_{\text{diff}}\right)$$

$$L_{\text{total}} = L_{\text{pred}} + L_{\text{diff}}$$

2.3.4. Multirepresentation Configuration

The multirepresentation configuration, inspired by the first place team, makes use of multiple simultaneous ways of encoding vertical profiles to help the model leverage complementary statistical views of the data. This is motivated by the heterogeneous statistical properties of atmospheric vertical profiles, where variables like moisture exhibit strong vertical gradients, skewness, and level-specific variability. Level-wise normalization preserves fine-grained vertical structure, column-wise normalization emphasizes global profile statistics (e.g., total column-integrated quantities), and the log-symmetric transform mitigates skewness in skewed distributions (common in microphysical variables) while preserving symmetry (Hu et al., 2025). This configuration only changes normalization for input variables and distinguishes between vertically-resolved variables x_{lev} and scalar (i.e., level-invariant) variables x_{scalar}. Scalar variables are normalized using standard z-scores. For vertically-resolved variables, we construct three parallel representations:

1. *Level-wise normalization*: Each feature at each vertical level is normalized using its own level-specific mean and standard deviation.
2. *Column-wise normalization*: Each vertically-resolved feature is normalized across all levels using a single global mean and standard deviation for that feature.
3. *Level-wise log-symmetric transformation*: A smooth, sign-preserving logarithmic transform (shown below) is applied to the levelwise-normalized features to reduce skewness while handling negative values.

$$x_{\text{log}} = \begin{cases} \log(x_{\text{lev}} - \alpha_{\text{lev}} + 1) & \text{where } x_{\text{lev}} \geq \alpha_{\text{lev}}, \\ -[\log(\alpha_{\text{lev}} - x_{\text{lev}} + 1)] & \text{where } x_{\text{lev}} < \alpha_{\text{lev}}, \end{cases}$$

In this case, α is defined separately for each vertically-resolved variable and vertical level. For a given variable x_{lev} with variable and level mean μ_{lev}, α_{lev} is equal to the minimum of $\left(\frac{x_{\text{lev}} - \mu_{\text{lev}}}{\mu_{\text{lev}}}\right)$ across all x_{lev} in the training data.

2.3.5. Expanded Variable List Configuration

The expanded variable list configuration appends inputs listed in Table 3 to the baseline set of input variables listed in Table 1. This expanded variable list matches the variable list used to achieve State-Of-The-Art (SOTA) results shown in Hu et al. (2025). These expanded input variables consist of tendencies and large-scale forcings at two timesteps as well as sin and cosine of latitude.

3. Results

3.1. Offline R^2 Comparison

In the Kaggle competition leaderboard, the winning solutions outperformed the U-Net submission by a considerable margin in offline R^2 skill. Surprisingly, this gap nearly vanishes after controlling for feature selection, preprocessing, normalization, training settings, postprocessing, and using individual models as opposed to ensembles. This is shown in Figure 2, which displays offline R^2 scores for both the standard configuration (depicted with dashed lines and hatched bar charts) and the expanded variable list configuration. A possible explanation for the large gap in the Kaggle competition is that the output normalization used by the U-Net resulted in worse performance (i.e., negative R^2) for stratospheric liquid cloud tendencies. While Hu et al. (2025) and this

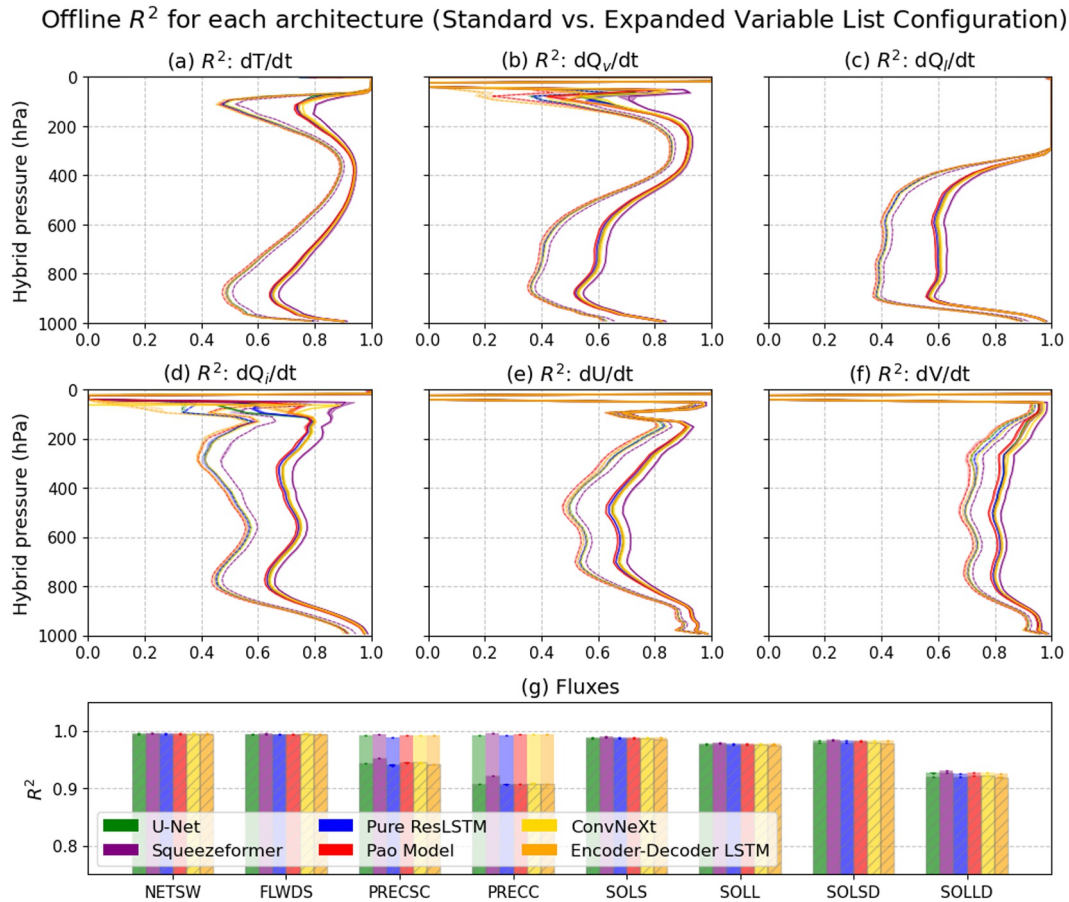

Figure 2. Offline R^2 values for each variable across architectures for the standard configuration (depicted using dashed lines and hatched bar charts) and the expanded variable list configuration (depicted using solid lines and semi-transparent shaded bar charts). For vertically-resolved variables, the colored lines depict the median R^2 while the shading shows the min and max across seeds for each architecture. For scalar variables, the bars show the medians while the vertical lines at the top of each bar show the min-max range. Subplots (a–f) refer to heating tendencies, moistening tendencies, liquid and ice cloud tendencies, and zonal wind tendencies. Subplot (g) refers to the following fluxes: net shortwave flux at surface (NETSW), downward longwave flux at surface (FLWDS), snow rate (liquid water equivalent) (PRECSC), rain rate (PRECC), downward visible direct solar flux to surface (SOLS), downward near-infrared direct solar flux to surface (SOLL), downward visible diffuse solar flux to surface (SOLSD), and downward near-infrared diffuse solar flux to surface (SOLLD).

work make use of a microphysics constraint that mirrors the one-moment microphysics scheme in the CRM to diagnose liquid and ice cloud tendencies as a function of total liquid and ice cloud tendency and temperature, Kaggle competitors coalesced around a "trick" that set stratospheric liquid cloud tendencies to $-\frac{q_l}{1200}$ (where q_l represents the amount of liquid cloud for a given unpredictable stratospheric level). This "trick" is based on the assumption that stratospheric moisture would tend to 0 (since there are 1,200 s in a GCM timestep). Finally, the best offline R^2 scores in this paper are not universally superior to those reported in Hu et al. (2025). Nevertheless, when controlling for the aforementioned factors, the Squeezeformer, which was used in the first place solution, shows clear positive separation from all architectures on all variables, and the reverse is true for the Pao Model, which was used in the third place solution. For all other architectures, the offline R^2 is less differentiated, with results varying based on variable and configuration. There is also very little variation in offline R^2 between seeds, as shown by the min-max shading for the vertically-resolved variables and the nearly invisible vertical lines showing min-max range for the scalar variables. Finally, as expected from previous work, there is a universal improvement to offline skill across architectures when expanding the input variable list to include variables like convective memory and large-scale forcings (Hu et al., 2025; Lin et al., 2025). The confidence loss, difference loss, and multirepresentation configurations yield smaller benefits compared to the offline R^2 of the standard configuration and are omitted from Figure 2 for visual clarity. However, as shown in Figure S3 in Supporting

19422466, 2026, 5, Downloaded from https://agupubs.onlinelibrary.wiley.com/doi/10.1029/2025MS005643 by Dtsch Zentrum F. Luft-U. Raum Fahrt In D. Helmholtz Gemein., Wiley Online Library on [27/10/2026]. See the Terms and Conditions (https://onlinelibrary.wiley.com/terms-and-conditions) on Wiley Online Library for rules of use; OA articles are governed by the applicable Creative Commons License

Information S1, the multirepresentation configuration yields large improvements in offline R^2, specifically for liquid cloud tendencies above 200 hPa and ice cloud tendencies above 400 hPa. This validates the idea that multiple complementary statistical views of the data can be useful for cloud mixing ratios, which have highly skewed distributions with long tails extending beyond 10 standard deviations (Hu et al., 2025). For completeness, we show how the confidence loss and difference loss configurations compare to the standard configuration in Figures S1 and S2 in Supporting Information S1, and we compare the models in the expanded variable list configuration to the models evaluated in Hu et al. (2025) in Figure S4 in Supporting Information S1.

3.2. Online Stability and Error Growth

Online, most architectures across configurations exhibit stable performance with minimal drift (i.e., systematic or growing errors), yet with some notable exceptions, as seen in Figure 3, which shows monthly RMSE for temperature and specific humidity across all configurations for each architecture. Monthly RMSE for other prognostic variables are shown in Figures S5, S6, S7, and S8 in Supporting Information S1, and the formula by which we calculate it is shown in Text S2 in Supporting Information S1. These results suggest that stability in the low-resolution real-geography ClimSim setting may be the default expectation going forward. We note that these results were obtained using the microphysics constraint by Hu et al. (2025), which was shown to improve online stability. Even so, cases of instability and drift still exist, and they arise for different architectures depending on choice of configuration.

In the standard configuration (Figures 3a and 3b), all hybrid simulations stably integrate without drift with the exception of those corresponding to the ConvNeXt architecture (yellow). Interestingly, this is achieved without the use of convective memory, inconsistent with previous experience by some of our team that had implicated this as important (albeit in a higher-resolution, aquaplanet setting using a different MMF version) in Lin et al. (2025).

In the confidence loss and difference loss configurations, we see the first signs of inter-seed variability in online stability and drift. In the confidence loss configuration, one of the seeds for the Encoder-Decoder LSTM experiences sustained high online temperature RMSE and one of the seeds for the Pao Model crashes due to numerical instability in the middle of the fourth simulation year. In the difference loss configuration, one of the seeds for the Pure ResLSTM architecture crashes in the middle of the fifth simulation year. Impactful inter-seed variability in online performance has been shown in prior work and is confirmed here, emphasizing the ongoing importance of training ensembles of ML parameterizations before drawing design conclusions (Han et al., 2023). Interestingly, the ConvNeXt architecture, which experienced significant online temperature error in the standard configuration, integrates stably without drift across all seeds in the confidence loss and difference loss configurations.

For the multirepresentation configuration (Figures 3g and 3h), the two architectures without convolutional elements—the Pure ResLSTM and the Encoder-Decoder LSTM—are the only ones to stably integrate without issue. Across the U-Net, ConvNeXt, and Pao Model architectures, every hybrid simulation experiences catastrophic drift or numerical instability. In the case of the Squeezeformer architecture, one of the hybrid simulations crashes from numerical instability within the first hundred simulation days and an annually recurring liquid cloud RMSE maximum emerges, consistent with systematic biases at a discrete phase of the seasonal cycle (Figure S6 in Supporting Information S1).

In the expanded variable list configuration, architectures that make repeated use of attention or LSTM elements are negatively impacted. The Squeezeformer architecture is worst affected, with hybrid simulations crashing in the first 10 simulation days. Meanwhile, only one out of three hybrid simulations using the Pao Model runs to completion, and the inter-seed variability in online temperature RMSE for both the Pure ResLSTM and the Encoder-Decoder LSTM is worsened. Conversely, hybrid simulations using the ConvNeXt architecture (which experiences catastrophic drift in the standard configuration) achieve best-in-class online temperature error in this configuration. Finally, the U-Net shows no signs of drift or numerical instability, although this was also the case in the standard configuration.

We excluded the fifth simulation year when assessing the online results for the expanded variable list configuration. This is because 10/18 hybrid simulations using this configuration encountered out-of-memory issues caused by our transition from the PyTorch-Fortran binding developed in Hu et al. (2025) to an FTorch binding (which makes use of CUDA GPU acceleration, resulting in a 4× speedup). In our implementation of the FTorch

19422466, 2026, 5, Downloaded from https://agupubs.onlinelibrary.wiley.com/doi/10.1029/2025MS005643 by Dtsch Zentrum F. Luft-U. Raum Fahrt In D. Helmholtz Gemein., Wiley Online Library on [27/10/2026]. See the Terms and Conditions (https://onlinelibrary.wiley.com/terms-and-conditions) on Wiley Online Library for rules of use; OA articles are governed by the applicable Creative Commons License

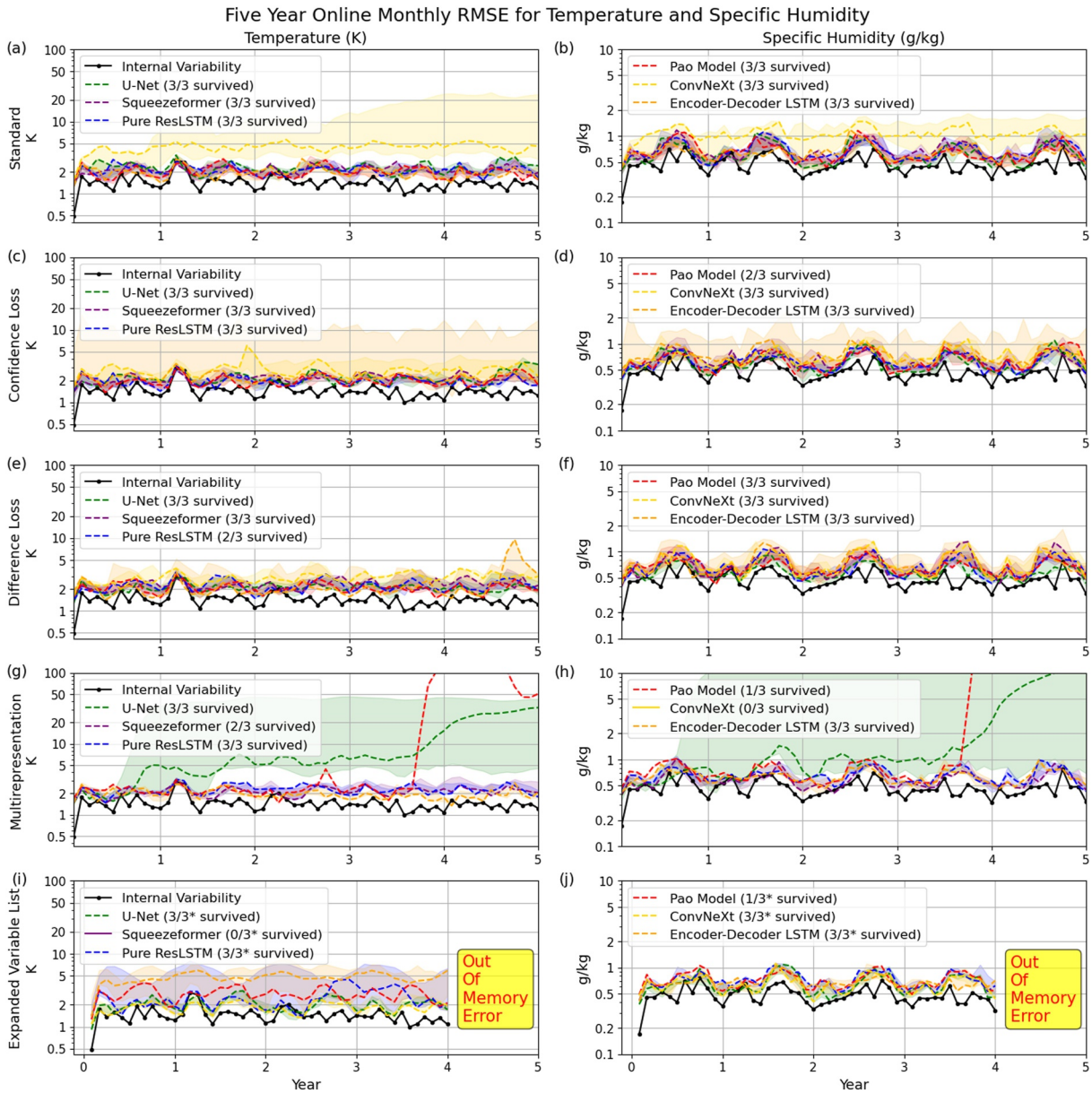

Figure 3. Online monthly Root Mean Squared Error (RMSE) for temperature and moisture for all architectures in each configuration. Shading indicates the inter-seed range (min to max RMSE across three seeds per month after excluding RMSE from hybrid simulations that crash at any point). Dashed lines show RMSE from the seed whose monthly mean absolute deviation from Multiscale Modeling Framework (MMF) RMSE is closest to the median absolute deviation across seeds. For visual clarity, RMSE for hybrid simulations that crash due to numerical instability are not shown. Internal variability is approximated via monthly RMSE when compared to another MMF simulation (which in general are not bit-for-bit reproducible). Subplots i and j only show data up to 4 years because of out-of-memory issues that caused most of the hybrid simulations to terminate in the middle of the fifth year. Asterisk (*) indicates that survival is assessed via integrating for four, and not five, simulation years.

binding, we neglected to make appropriate use of `torch_delete` (which is now automated in newer versions of FTorch), introducing out-of-memory issues. Nevertheless, based on the self-similarity of most seasonal RMSE variations we do not believe curtailing the simulations at 4 years significantly impacts our conclusions, and, in general, we use 4-year simulations when comparing configurations and 5-year simulations when directly comparing our online results to those seen in Hu et al. (2025).

19422466, 2026, 5, Downloaded from https://agupubs.onlinelibrary.wiley.com/doi/10.1029/2025MS005643 by Dtsch Zentrum F. Luft-U. Raum Fahrt In D. Helmholtz Gemein., Wiley Online Library on [27/10/2026]. See the Terms and Conditions (https://onlinelibrary.wiley.com/terms-and-conditions) on Wiley Online Library for rules of use; OA articles are governed by the applicable Creative Commons License

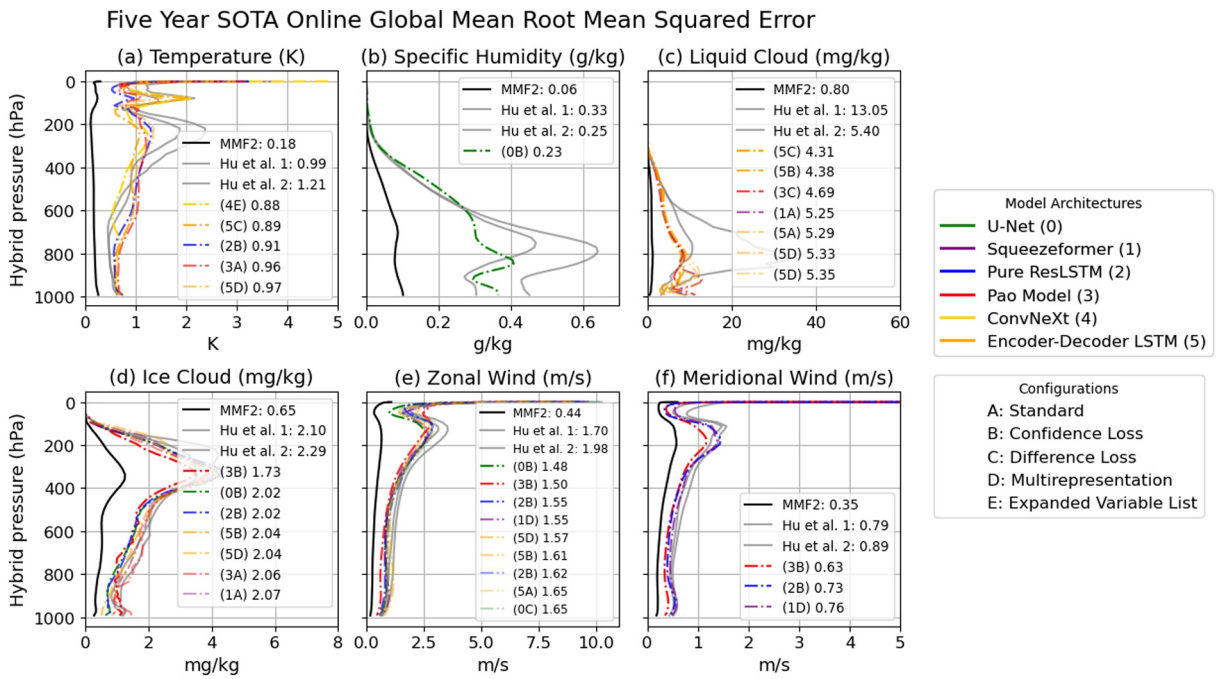

Figure 4. Vertical profiles of online global Root Mean Squared Error across (a) temperature, (b) specific humidity, (c) liquid cloud, (d) ice cloud, (e) zonal wind, and (f) meridional wind for architectures that surpass those of the U-Net shown in Hu et al. (2025). Each subplot contains a legend that uses a number and letter to denote the architecture and configuration corresponding to each vertical profile.

3.3. SOTA Online Results and a Revealed Persistent Secondary Bias

Regarding online 5 year global RMSE, no single hybrid simulation yields a simultaneous improvement over the best results in Hu et al. (2025) across all field variables of temperature, liquid cloud, ice cloud, zonal wind, and meridional wind. However, Kaggle-inspired architectures and design decisions did lead to state-of-the-art (SOTA) variable-specific results, as seen in Figure 4. For the lowest online RMSE achieved by all hybrid simulations in each category, we see an 11.1% improvement for temperature, 8% improvement for moisture, 20.2% improvement for liquid cloud, 17.6% improvement for ice cloud, 12.9% improvement for zonal wind, and 20.3% improvement for meridional wind, relative to results from Hu et al. (2025). For online moisture RMSE, only one of 90 hybrid simulations outperforms the best results from Hu et al. (2025). This simulation uses the same U-Net architecture but with our confidence loss configuration. For online liquid cloud RMSE, five out of seven hybrid simulations that achieve a lower RMSE than Hu et al. (2025) make use of the Encoder-Decoder LSTM architecture. These results could suggest that different architectures are better suited at emulating different tendencies; however, confirming this hypothesis and understanding associated mechanisms would require a more targeted study with greater sampling of the online consequences of intrinsic ML uncertainties (Lin et al., 2025).

In Figure 5, we show the online zonal mean biases corresponding to the hybrid simulations with state-of-the-art online 5 year global RMSE for temperature, specific humidity, zonal wind, liquid cloud, ice cloud, heating tendencies, moistening tendencies, liquid and ice cloud tendencies, and zonal wind tendencies. While some of these zonal mean biases represent substantial improvements over those seen in Hu et al. (2025), the overall structure of these biases persists. Online zonal mean biases with similar structure (e.g., warm bias at higher altitudes over the poles) have also been reported in multiple independent studies (e.g., Hu et al., 2025; Iglesias-Suarez et al., 2024; Lin et al., 2025; Rasp et al., 2018; Wang et al., 2022) and are *nearly universal* for all online simulations conducted in this study. As an illustrative example, we show the online zonal mean temperature and moisture biases for different architectures in the confidence loss configuration using a common seed in Figure 6. A similar phenomenon exists across all variables, as seen in Figures S9–S12 in Supporting Information S1.

In addition to exhibiting similar zonal mean biases, all architectures across all configurations systematically underpredict both the global average and standard deviation of precipitable water online, particularly in the

19422466, 2026, 5, Downloaded from https://agupubs.onlinelibrary.wiley.com/doi/10.1029/2025MS005643 by Dtsch Zentrum F. Luft-U. Raum Fahrt In D. Helmholtz Gemein., Wiley Online Library on [27/10/2026]. See the Terms and Conditions (https://onlinelibrary.wiley.com/terms-and-conditions) on Wiley Online Library for rules of use; OA articles are governed by the applicable Creative Commons License

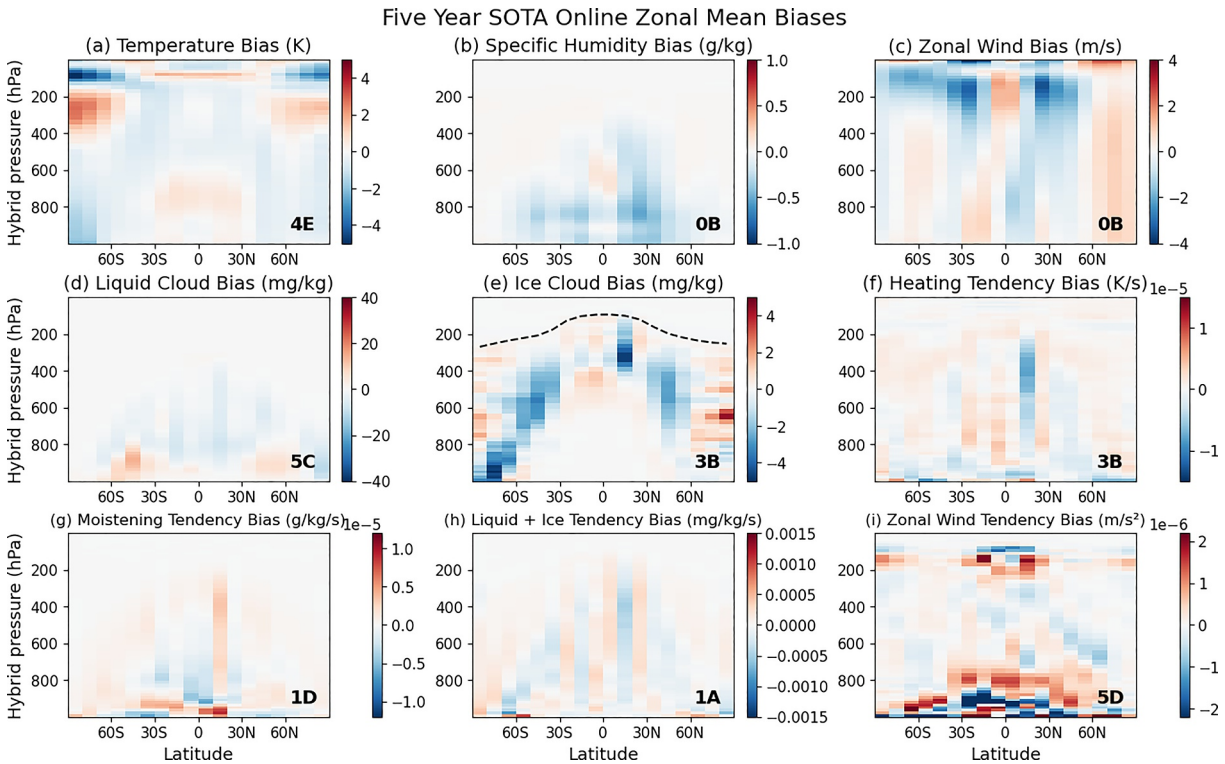

Figure 5. Online zonal mean bias for the architectures with the lowest global Root Mean Squared Error. In a similar fashion to Figure 4, the architecture and configuration responsible for each zonal mean bias plot is denoted with a number-letter combination where the numbers (0–6) corresponds to the choice of architecture (i.e., U-Net, Squeezeformer, Pure ResLSTM, Pao Model, ConvNeXt, and Encoder-Decoder Long Short-Term Memory, respectively) while the letters (A–E) corresponds to the choice of configuration (i.e., standard, confidence loss, difference loss, multirepresentation, and expanded variable list, respectively).

tropics, as seen in Figure 7 and Figure S13 in Supporting Information S1. Precipitation extremes are also underestimated across architectures in the standard configuration; however, this is partially mitigated in the expanded variable list configuration, as seen in Figure 8. Corresponding figures for other configurations are shown in Figures S14, S15, and S16 in Supporting Information S1. In line with the findings from Hwong et al. (2023); Shamekh et al. (2023); Beucler et al. (2025), we hypothesize that the improved representation of precipitation extremes when using an expanded variable list may stem from the ability of convective memory to provide more information about underlying subgrid-scale cloud structure and organization Colin et al. (2019). If so, future work could improve performance on precipitation extremes by making the ML parameterizations inherently stochastic and more explicitly incorporating CRM state information, which persists between time steps but is currently excluded from ML inputs due to data volume constraints (Christensen et al., 2024; Leutbecher et al., 2017; Schneider et al., 2024). An alternative explanation could be that the expanded variable list also offers large-scale forcings, which provide additional information about the overall model state prior to running the dynamical core. However, a more detailed ablation study of the expanded variables would be needed to understand the actual cause.

3.4. Universal Offline Biases

Pathologies that transcend the choice of architecture are even more pronounced offline. Because offline errors compound across timesteps online, offline biases are a natural suspect for stubborn online biases. Offline zonal mean biases across vertically-resolved variables are remarkably similar across seeds, architectures, and configurations, as seen in Figure 9 and SI Figures S17-S45 in Supporting Information S1. For offline moistening, these biases are strongest in the tropics with a wet bias near the surface and dry bias higher in the atmosphere. Figure 9 and the aforementioned SI figures also reveal the state-dependent nature of this bias, whose magnitude increases with convective activity (approximated here using precipitation percentile). This is in line with findings from Heuer et al. (2025), who showed that the ML parameterization was most "uncertain" in moist, unstable

19422466, 2026, 5, Downloaded from https://agupubs.onlinelibrary.wiley.com/doi/10.1029/2025MS005643 by Dtsch Zentrum F. Luft-U. Raum Fahrt In D. Helmholtz Gemein., Wiley Online Library on [27/10/2026]. See the Terms and Conditions (https://onlinelibrary.wiley.com/terms-and-conditions) on Wiley Online Library for rules of use; OA articles are governed by the applicable Creative Commons License

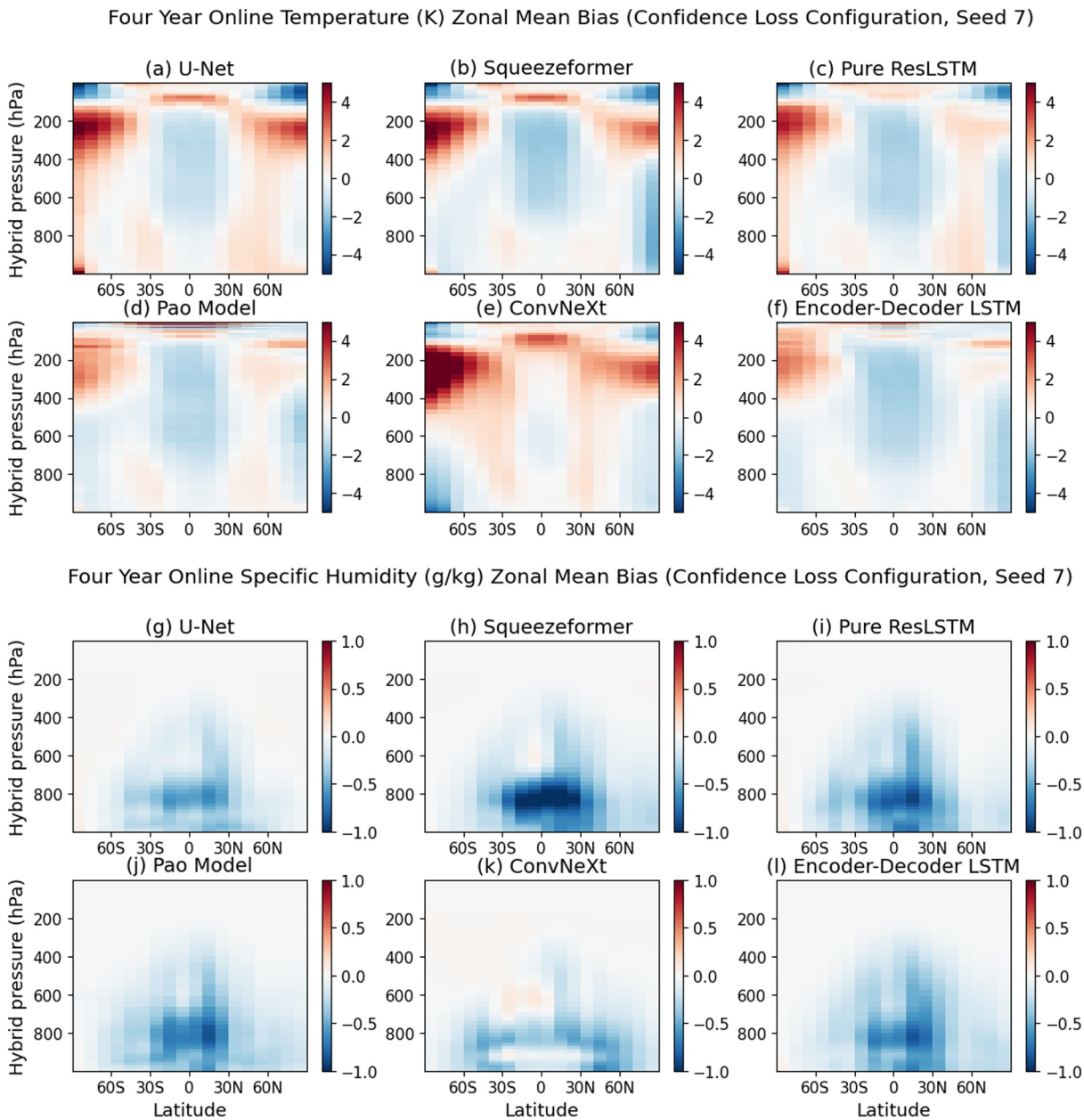

Figure 6. This figure shows online zonal mean biases for temperature and moisture across architectures in the confidence loss configuration, trained using a common seed.

conditions, which occur more frequently in lower latitudes. Interestingly enough, the direction of this bias is consistent across seeds, architectures, and configurations, indicating that offline biases are a systemic issue that is unlikely to be resolved by simply using a more sophisticated deterministic architecture. We did not expect to find such self-similar offline biases across the top architectures in the Kaggle leaderboard, which could be viewed as a limitation of the R^2-based reward metric used in the competition. This could also be viewed as motivation to explicitly penalize zonal mean bias in the loss function to avoid the accumulation of systematic biases online. This is analogous in aim, though not in type of bias, to the penalization of spectral bias in Kochkov et al. (2024).

Multiple other variables like zonal and meridional wind tendencies also show state-dependent universal offline biases, but there are also exceptions. e.g., the offline zonal mean heating tendency bias is greatly reduced and loses its distinctive structure (i.e., a cooling bias over the tropics) with an expanded variable list. When it comes to

19422466, 2026, 5, Downloaded from https://agupubs.onlinelibrary.wiley.com/doi/10.1029/2025MS005643 by Dtsch Zentrum F. Luft-U. Raum Fahrt In D. Helmholtz Gemein., Wiley Online Library on [27/10/2026]. See the Terms and Conditions (https://onlinelibrary.wiley.com/terms-and-conditions) on Wiley Online Library for rules of use; OA articles are governed by the applicable Creative Commons License

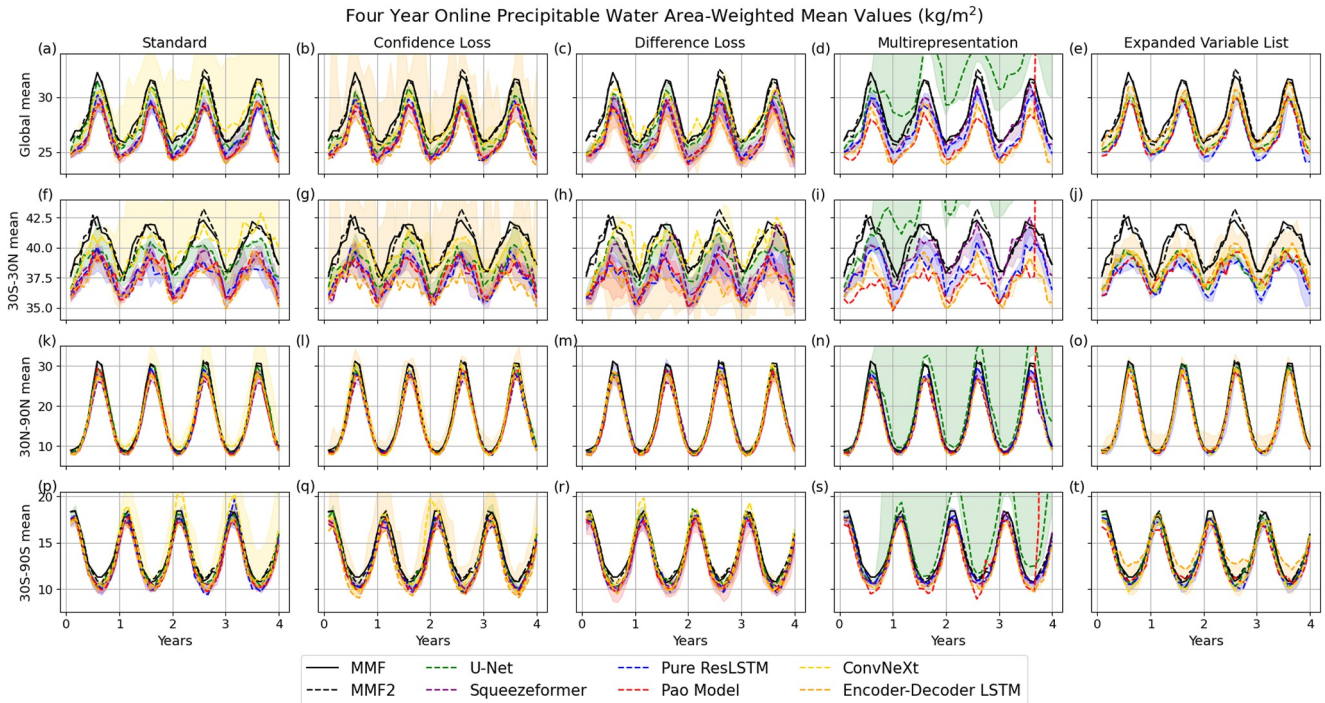

Figure 7. Four-year area-weighted mean values for precipitable water in four regions (global, 30 S–30N, 30N–90N, and 30S–90S) for all architectures across all configurations. Solid and dashed black lines show two independent Multiscale Modeling Framework (MMF) reference simulations. For each architecture and configuration combination, shading depicts the min-to-max range across seeds, and the dashed colored line shows the median-performing seed by mean absolute difference from MMF.

offline liquid and ice cloud tendency biases, those are indeed seemingly universal across all models trained in this study. However, such biases were not seen when evaluating predictions produced directly by the first and second place Kaggle teams (shown in Figures S46 and S47 in Supporting Information S1). A plausible cause for this discrepancy is the use of the microphysics constraint developed by Hu et al. (2025) as it was implemented across all of our models but not used by the Kaggle competitors. However, a more thorough ablation is required to fully confirm this hypothesis.

3.5. Offline Training and Online Simulation Computational Efficiency

In addition to being able to accurately emulate the coarse-grained effects of subgrid physics in MMF, we would like ML parameterizations to be able to do so efficiently. To measure tradeoffs between these competing priorities, we evaluate 5 year online global mean RMSE against Simulation Years Per Day (SYPD) in Figures 10a–10f. In our case, all online simulations are run with GPU acceleration on 8 NVIDIA A100 GPUs using an FTorch binding. The reference MMF simulation is also GPU accelerated, and achieves 9.9 SYPD (Hu et al., 2025). While earlier figures comparing online error across different variables were mostly ambiguous with regards to which architectures were more performant, a clearer hierachy emerges with SYPD. The U-Net and Pure ResLSTM show similar SYPD, but they are surpassed by the Pao Model which is in turn surpassed by the Encoder-Decoder LSTM and finally by the ConvNeXt architecture. It is important to note that this hierarchy is not predictable a priori using the respective trainable parameter count for each architecture, shown in Figure 10g. For example, the U-Net and Pure ResLSTM have lower trainable parameter counts and lower SYPD than all other architectures evaluated in this study. By contrast, the ConvNeXt architecture has the second highest trainable parameter count and achieves the highest SYPD across all architectures. When it comes to training time, the number of trainable parameters is critical (as seen in Figures 10g and 10h), but it is still not perfectly predictive of computational performance. For example, the Encoder-Decoder LSTM has ∼43% more trainable parameters than the U-Net but takes roughly the same amount of time to train.

19422466, 2026, 5, Downloaded from https://agupubs.onlinelibrary.wiley.com/doi/10.1029/2025MS005643 by Dtsch Zentrum F. Luft-U. Raum Fahrt In D. Helmholtz Gemein., Wiley Online Library on [27/10/2026]. See the Terms and Conditions (https://onlinelibrary.wiley.com/terms-and-conditions) on Wiley Online Library for rules of use; OA articles are governed by the applicable Creative Commons License

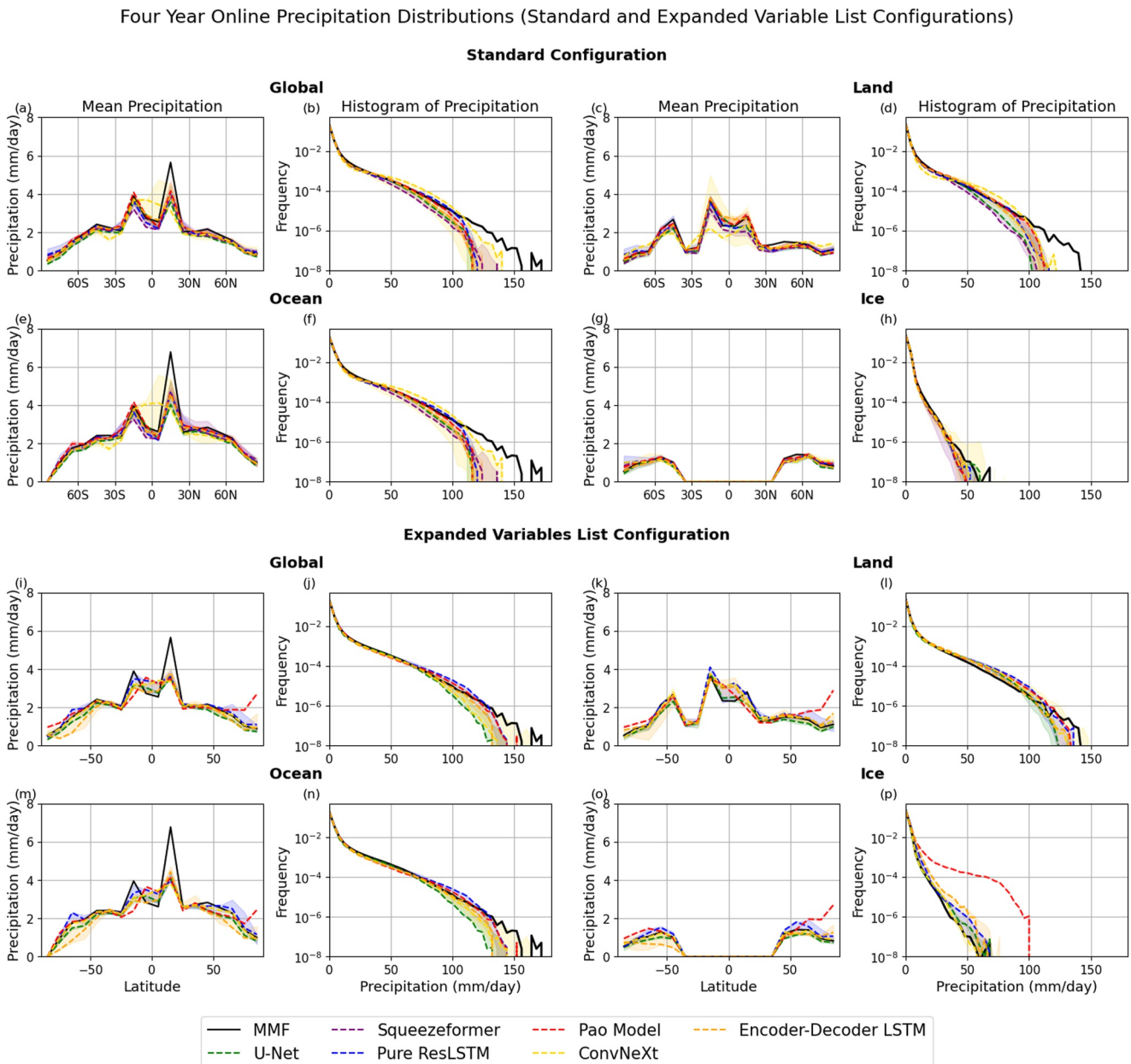

Figure 8. Four-year online precipitation distributions for the standard (top half) and expanded variable list (bottom half) configurations. Each configuration block shows four surface types (global, land, ocean, and ice), with paired subplots per surface type: zonal mean precipitation (mm/day) as a function of latitude (left) and an area-weighted histogram of hourly precipitation on a log-frequency scale (right). The solid black line shows the Multiscale Modeling Framework reference simulation. For each architecture, shading depicts the min-to-max range across seeds, and the dashed colored line shows the median-performing seed by mean absolute difference from the median.

When looking at which architectures strike the best balance between online accuracy and computational efficiency, Figure 10 shows that the Encoder-Decoder LSTM performs favorably across multiple variables. Indeed, multiple hybrid simulations with Encoder-Decoder LSTMs achieve lower online global mean RMSE than that seen in Hu et al. (2025) for temperature, liquid cloud, ice cloud, and zonal wind. However, in the case of moisture, hybrid simulations using the U-Net architecture consistently demonstrate lower online RMSE, as evidenced by Figures 4b and 10b. Nevertheless, we believe that the high SYPD and competitive RMSE achieved by the Encoder-Decoder LSTM warrant the use of this architecture as a reasonable baseline in future work.

19422466, 2026, 5, Downloaded from https://agupubs.onlinelibrary.wiley.com/doi/10.1029/2025MS005643 by Dtsch Zentrum F. Luft-U. Raum Fahrt In D. Helmholtz Gemein., Wiley Online Library on [27/10/2026]. See the Terms and Conditions (https://onlinelibrary.wiley.com/terms-and-conditions) on Wiley Online Library for rules of use; OA articles are governed by the applicable Creative Commons License

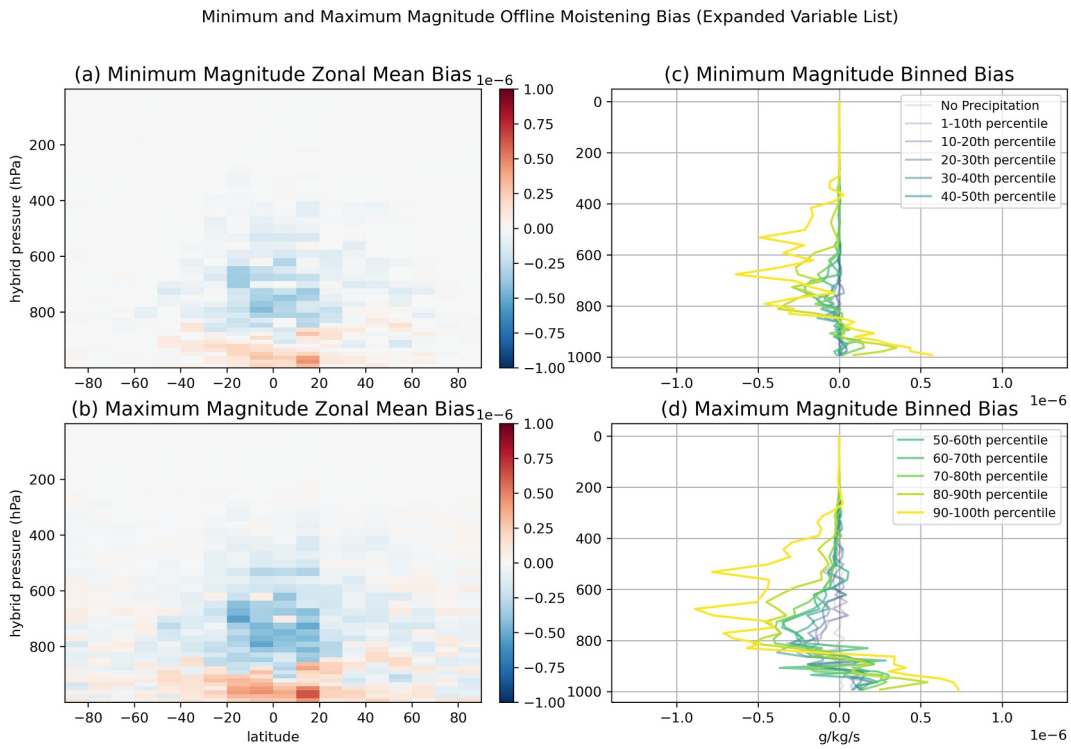

Figure 9. Panels (a) and (b) show the minimum and maximum offline zonal-mean moistening tendency biases across the expanded variable list configuration. The minima and maxima are calculated over the architecture dimension after averaging across seeds. Panels (c) and (d) show the minima and maxima of the vertical profiles of these biases binned by precipitation percentile (also after averaging across seeds).

It is important not to overthink this preliminary assessment of the computational trade-offs of these architecture implementations, which we readily admit were approached pragmatically for research purposes and not performance optimization. There is a rich tradition of inefficient research prototyping followed by impactful performance optimizations in the ML literature, and it is logical to expect that the SYPD hierarchy depicted in this paper would change if the implementations of these architectures were optimized for target hardware. That said, the hierarchy shown could prove to be representative and, at the very least, points to tradeoffs that are readily apparent with existing implementations in the software repository attached to this paper. Benchmark competitions that directly reward model simplicity or efficiency could be an interesting path to discovering more Pareto-optimal architectures (Heuer et al., 2025).

4. Conclusion

We implemented, trained, and prognostically tested 90 ML parameterizations of cloud resolving physics of turbulence, radiation, and moist convection, inspired by a subset of novel architectures and design decisions pioneered by the winning teams in the 2024 ClimSim Kaggle competition.

The results reveal previously unprecedented skill across multiple independent online metrics of prognostic error, confirming our working hypothesis that organized benchmarks can lead to measurable progress for hybrid climate simulation even when formulated as offline training strategies.

Online stability with tolerable drift, which has been difficult to achieve in the limit of MMF CRM emulation, especially when including full microphysical emulation and land surface feedback, now appears to be reproducible with multiple architecture and design decision combinations, at least in the low-resolution real-geography ClimSim setup we have explored, which we consider an important milestone.

Despite the large diversity in architectures sampled, we have also identified unexpectedly systematic secondary biases that could speak to deeper issues of the MMF emulation problem design. These stubborn symptoms include

19422466, 2026, 5, Downloaded from https://agupubs.onlinelibrary.wiley.com/doi/10.1029/2025MS005643 by Dtsch Zentrum F. Luft-U. Raum Fahrt In D. Helmholtz Gemein., Wiley Online Library on [27/10/2026]. See the Terms and Conditions (https://onlinelibrary.wiley.com/terms-and-conditions) on Wiley Online Library for rules of use; OA articles are governed by the applicable Creative Commons License

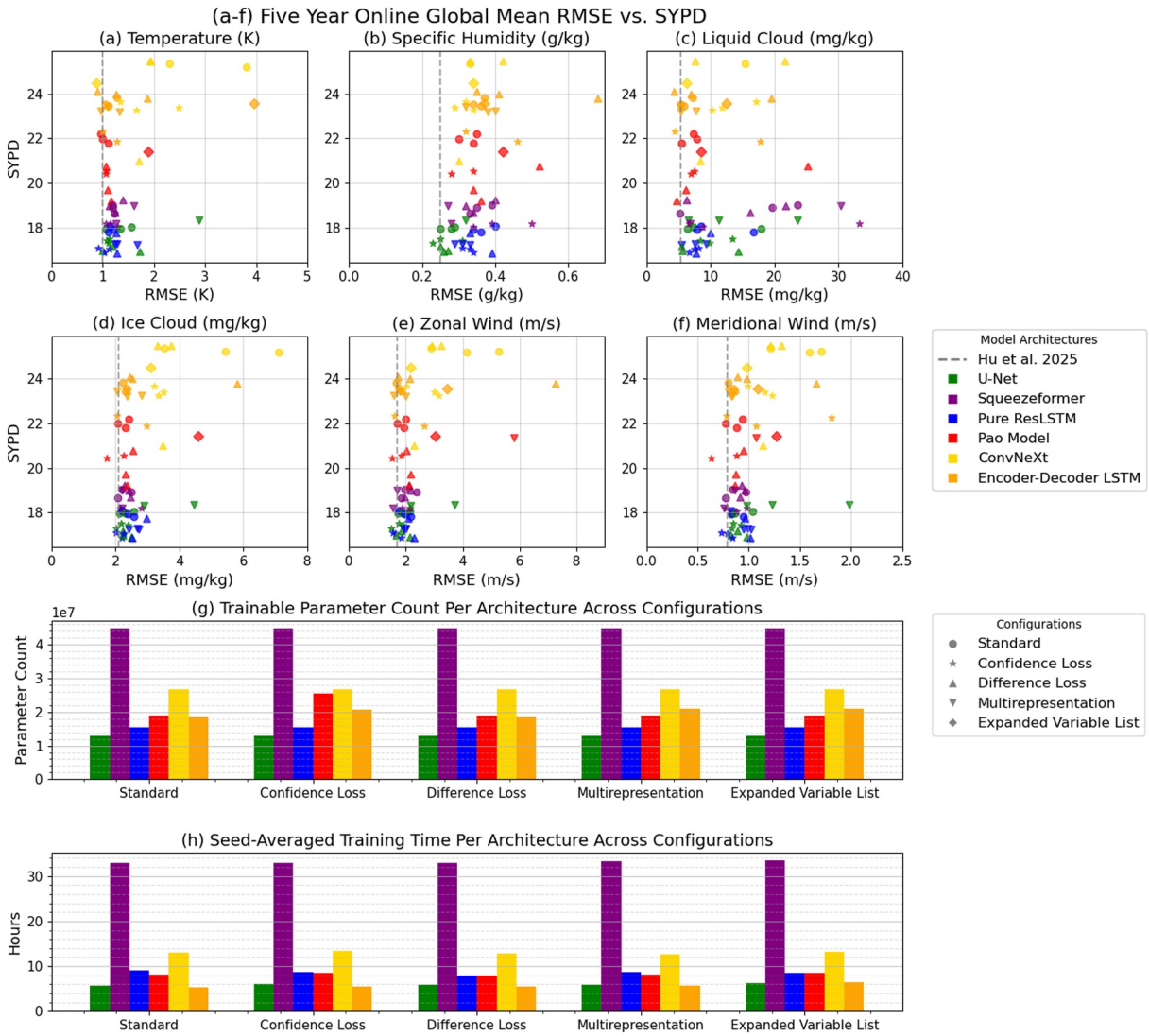

Figure 10. (a–f) shows Simulation Years Per Day versus Global Mean Root Mean Squared Error (RMSE) for temperature, specific humidity, liquid cloud, ice cloud, zonal wind, and meridional wind for all hybrid simulations that integrated 5 years. The best 5 year Global Mean RMSE for each variable from Hu et al. (2025) is depicted with a dashed vertical line for reference. Panel (g) shows the number of trainable parameters for each architecture and configuration, and panel (h) shows the seed-averaged training time for each architecture and configuration combination. Each model was trained using a Distributed Data Parallel strategy across four NVIDIA A100 GPUs, and each online simulation was conducted with GPU acceleration across eight NVIDIA A100 GPUs.

time mean online temperature bias patterns and systematic online underprediction of precipitable water in the tropics and precipitation extremes in general. Targeting the shared offline and online biases that transcend the choice of seed, architecture, and configuration may be the next frontier for hybrid physics-ML climate simulation in the low-resolution real-geography setting. However, certain aspects of online performance, like variation stemming from inter-seed variability, are still best described as emergent properties, and prioritizing the treatment of the more deterministic offline biases may be the more efficient avenue for continued progress. It is possible that the shared failure modes described in this paper are escaped when deviating from the factors we controlled for to facilitate easier inter-comparisons. However, a more straightforward means of directly addressing systematic biases may be to explicitly include a bias penalty in the loss function (Kochkov et al., 2024). Kochkov et al. (2024) used a multi-component loss function that penalized spectral bias, but this was done in the context of end-to-end online training to prevent accumulation of errors across timesteps. Finally, we expect including information about subgrid-scale cloud structure and organization in the input to also reduce systematic errors (Beucler et al., 2025; Colin et al., 2019; Hwong et al., 2023; Shamekh et al., 2023).

19422466, 2026, 5, Downloaded from https://agupubs.onlinelibrary.wiley.com/doi/10.1029/2025MS005643 by Dtsch Zentrum F. Luft-U. Raum Fahrt In D. Helmholtz Gemein., Wiley Online Library on [27/10/2026]. See the Terms and Conditions (https://onlinelibrary.wiley.com/terms-and-conditions) on Wiley Online Library for rules of use; OA articles are governed by the applicable Creative Commons License

When comparing architectures, drawing empirically robust conclusions is complicated by the fact that only three seeds were trained for each architecture and configuration pair. Nevertheless, our results in Figures 3 and 4 suggest emerging patterns that we believe warrant further investigation in future work. Rather than presenting these observations as definitive findings, we highlight them here to generate questions for future research, focusing on aspects of the ML part of the problem that can be investigated without enhancements to the underlying ClimSim benchmark data:

Observation #1

Observation:

The U-Net achieves the lowest online moisture error across all architectures, and none of the competing architectures surpass the online moisture error from the best U-Net in Hu et al. (2025).

Motivated Question:

Are there multi-scale mechanisms utilized by the U-Net that make it particularly well-suited for reduced online moisture biases? To what extent are these mechanisms portable to other architectures?

Observation #2

Observation:

Different architectures respond differently online to different design decisions. For example, results shown in Figure 3 hint that input variable expansion may favor architectures with purely convolutional elements while multirepresentation may favor architectures with purely recurrent NN elements.

Motivated Question:

What makes various architectures respond differently to design decisions online? Is the online response to a given design decision entirely emergent or can it be predicted ahead of time?

Observation #3

Observation:

Some architectures seem to have greater inter-seed online variability than others. For example, while some hybrid simulations using the Encoder-Decoder LSTM architecture strike a favorable balance between SYPD and global mean RMSE relative to those from other architectures, this is not universally the case across seeds.

Motivated Question:

Are there ways to reduce inter-seed online variability and improve the reliability of hybrid physics-ML climate simulations? Which architectural components are most sensitive to weight initialization?

Observation #4

Observation:

Architectures that used transformer-encoder elements, like the Squeezeformer and Pao Model, experienced numerical instability across almost all seeds in the expanded variable list configuration.

Motivated Question:

19422466, 2026, 5, Downloaded from https://agupubs.onlinelibrary.wiley.com/doi/10.1029/2025MS005643 by Dtsch Zentrum F. Luft-U. Raum Fahrt In D. Helmholtz Gemein., Wiley Online Library on [27/10/2026]. See the Terms and Conditions (https://onlinelibrary.wiley.com/terms-and-conditions) on Wiley Online Library for rules of use; OA articles are governed by the applicable Creative Commons License

> Does learning potentially unphysical non-vertically-local patterns that fail to generalize online make transformer-encoder elements ill-suited for ML parameterization (compared to more traditional convolutional or recurrent NN layers)?

Democratizing the problem of hybrid physics-ML climate simulation in the context of MMF to the ML and data science community on Kaggle has yielded new insights that narrow the still-formidable gap between proof-of-concept and operational capability. Being such a large-scale competition, the Kaggle competition offered arguably the largest search across ML architectures that has been carried out for Earth system parameterizations. It is interesting that the winning models were primarily composed of NN based architectures, suggesting that today's modern NNs offer the best flexibility for modeling the highly complex phenemomena within a grid-cell. This contrasts with other Kaggle competitions (particularly ones centered around tabular data sets) in which lower complexity models such as random forests and gradient boosted trees were able to outcompete higher complexity NNs, which can be biased to overly smooth solutions (Grinsztajn et al., 2022; Januschowski et al., 2022). This affirms the idea that ML parameterization development is a complex and nonlinear enough problem to deserve complex NN based architectures going forward. Unfortunately, the emergent discrepancy between offline and online skill limits the degree to which crowdsourced solutions tailored to a singular offline benchmark can be relied upon for breakthrough progress online.

Although we achieve new SOTA values across multiple online metrics in this study, no single hybrid simulation conducted here presents a pareto-improvement over online results from Hu et al. (2025). Instead, our main contributions are demonstrating that stable and accurate online simulations are reproducibly achievable across diverse architectures going forward and identifying universal failure points and emerging patterns worthy of exploration in future research. With the democratization of the online aspect of this problem via ClimSim-Online and the identification of universal offline and online failure modes, we expect follow-up work to result in rapid, continued progress (Yu et al., 2025).

Looking ahead, such progress may eventually result in reproducibly stable, high-resolution hybrid simulations with minimal bias or drift within the ClimSim framework. However, actual downstream impact (in the form of a hybrid physics-ML climate model usable for operational climate simulation) will inevitably require moving beyond the confines of the current ClimSim benchmark data set, and potentially MMF in general. Although ClimSim has already facilitated remarkable progress in hybrid physics-ML climate modeling and will likely continue to do so going forward, the MMF it is based around also possesses significant limitations. Chief among them is the lack of support for aerosol-cloud interaction in the GPU-enabled version of E3SM-MMF—a deficiency that will only be addressed with additional funding. Provided this is fixed, there are other limitations that are likely best addressed with a new data set, benchmarks, containerized climate model, and online competition. In Heuer et al. (2025), the fact that radiative and convective tendencies were not separated in ClimSim meant that the authors had to subtract radiative tendencies by approximating them using the "RTE + RRTMGP" scheme (Pincus et al., 2019, 2023). In Beucler et al. (2021), the authors developed analytically constrained NNs that enforced conservation laws to within machine precision. However, this is not currently possible with the current variable list, which is missing top of atmosphere radiative energy fluxes. Top of atmosphere irradiance would also allow for incorporating the influence of cloud radiative effects, which have been shown to be important for accurately representing extreme rainfall (Medeiros et al., 2021). Prior work has also shown the utility of multiclimate data for training, validation, testing, and developing or learning climate-invariant feature transformations (Clark et al., 2022; Bhouri et al., 2023; Lin et al., 2025; S. Liu & O'Gorman, 2025; Han et al., 2025). Unfortunately, ClimSim only contains data from a single climate. Additionally, detecting differences in emergent online behavior with sufficient statistical power can require large (O(100)) ensembles, motivating the inclusion of even simpler climate models that can facilitate online testing with large sample sizes without inordinate computational expense (Lin et al., 2025; Mansfield et al., 2023).

Nevertheless, the long-term ambition of hybrid physics-ML climate modeling is to potentially *exceed*, and not just match, the accuracy of the expensive physics-based simulations on which such models are trained. Encouragingly, data-driven emulators for weather and PDE systems have in some cases even demonstrated the ability to outperform their own training data (Christensen et al., 2026; Koehler & Thuerey, 2025), and hybrid physics-ML climate models designed from the ground up to be end-to-end differentiable (e.g., Kochkov et al. (2024);

19422466, 2026, 5, Downloaded from https://agupubs.onlinelibrary.wiley.com/doi/10.1029/2025MS005643 by Dtsch Zentrum F. Luft-U. Raum Fahrt In D. Helmholtz Gemein., Wiley Online Library on [27/10/2026]. See the Terms and Conditions (https://onlinelibrary.wiley.com/terms-and-conditions) on Wiley Online Library for rules of use; OA articles are governed by the applicable Creative Commons License

Davenport et al. (2026)) enable direct training on observational data in ways that are extremely impractical or impossible for conventional Fortran-based physics models (Yuval et al., 2026). Moreover, there is some emerging evidence suggesting that NN parameterizations may be capable of generalizing across climates and even across climate models (Han et al., 2025; Heuer et al., 2025). In Han et al. (2025), the authors showed for the first time that a NN parameterization trained exclusively on simulation data using present-day SSTs could produce a stable, decadal hybrid GCM simulation under a +4K SST warm climate with real geography, accurately reproducing climate responses across thermodynamic states, circulations, and extreme precipitation. In Heuer et al. (2025), the authors successfully coupled a ML convective parameterization—trained on high-resolution ClimSim data with a Kaggle-inspired architecture—to ICON, achieving stable 20-year AMIP simulations. Such cross-model transferability is particularly promising for future work, as mastering hybrid simulation with MMF may be a necessary stepping stone toward achieving success in the harder problem of hybrid simulations using coarse-grained GCRMs. Unlike MMF, GCRMs eliminate not only the convenient scale-separation used for ML parameterizations but also the unnatural artifacts caused by the inability of the large-scale GCM flow to advect small-scale CRM fluctuations (Pritchard et al., 2011; Brenowitz & Bretherton, 2019; Brenowitz et al., 2020; W. M. Hannah et al., 2020; Jansson et al., 2022; W. Hannah & Pressel, 2022; Heuer et al., 2024; Schneider et al., 2024; Heuer et al., 2025). The progress reported here—spanning crowdsourced architecture discovery, reproducibly stable online integration, and systematic failure-mode analysis—is yet another important step toward this grander ambition.

Conflict of Interest

The authors declare no conflicts of interest relevant to this study.

Availability Statement

The GitHub repository associated with this work is available via Apache License 2.0 and developed openly at https://github.com/leap-stc/climsim-kaggle-edition. The version of E3SM-MMF made compatible with FTorch is available at https://github.com/leap-stc/E3SM_nvlab. All experiments were run on NVIDIA A100 GPUs. Approximately 4,477 GPU-hours were used for training, 3,833 GPU-hours were used for online simulation, and less than 10 GPU-hours were used for offline inference. In total, we estimate 8,320 GPU-hours were used to conduct this study. All models, checkpoints, and normalization files are uploaded to Hugging Face and are available at https://hf.co/collections/jlin404/climsim-kaggle-models. Software repositories, online simulation output, and various online simulation metadata are preserved at https://zenodo.org/records/18883121.

Acknowledgments
This work is primarily funded by National Science Foundation (NSF) Science and Technology Center (STC) Learning the Earth with Artificial Intelligence and Physics (LEAP), Award 2019625-STC. High-performance computing was conducted on NERSC Perlmutter. T. Beucler acknowledges funding from the Swiss State Secretariat for Education, Research and Innovation (SERI) for the Horizon Europe project AI4PEX (Grant agreement ID: 101137682 and SERI no 23.00546). H. Christensen acknowledges funding through a Leverhulme Trust Research Leadership Award, and from the UK Research and Innovation (UKRI) under the UK government's Horizon Europe funding guarantee (Grant 10049639) to support the Horizon Europe EERIE project (Grant agreement no 101081383) funded by the European Union. W. Hannah acknowledges support for their contribution to this work from the U.S. Department of Energy by Lawrence Livermore National Laboratory under Contract DE-AC52-07NA27344. H. Heuer received funding for this study from the European Research Council (ERC) Synergy Grant "Understanding and Modeling the Earth System with Machine Learning (USMILE)" under the Horizon 2020 research and innovation programme (Grant agreement no. 855187). Views and opinions expressed are however those of the author(s) only and do not necessarily reflect those of the European Union or the European Climate Infrastructure and Environment Executive Agency (CINEA). Neither the European Union nor the granting authority can be held responsible for them. We are thankful to the Kaggle staff who made this competition possible, in particular Ashley Chow, Walter Reade, and Maggie Demkin, and to the anonymous reviewers at JAMES for their constructive comments and careful attention to detail. We also extend our gratitude to the hundreds of Kaggle participants who contributed their time and brilliant ideas to pushing science forward.

References

Atkinson, J., Elafrou, A., Kasoar, E., Wallwork, J. G., Meltzer, T., Clifford, S., et al. (2025). FTorch: A library for coupling PyTorch models to fortran. *Journal of Open Source Software*, *10*(107), 7602. https://doi.org/10.21105/joss.07602

Beucler, T., Grundner, A., Shamekh, S., Ukkonen, P., Chantry, M., & Lagerquist, R. (2025). Distilling machine learning's added value: Pareto fronts in atmospheric applications. *Artificial Intelligence for the Earth Systems*, *4*(2), e240078. https://doi.org/10.1175/AIES-D-24-0078.1

Beucler, T., Pritchard, M., Rasp, S., Ott, J., Baldi, P., & Gentine, P. (2021). Enforcing analytic constraints in neural networks emulating physical systems. *Physical Review Letters*, *126*(9), 098302. https://doi.org/10.1103/physrevlett.126.098302

Bhouri, M. A., Peng, L., Pritchard, M. S., & Gentine, P. (2023). *Multi-fidelity climate model parameterization for better generalization and extrapolation*. arXiv.org.

Bonev, B., Kurth, T., Mahesh, A., Bisson, M., Kossaifi, J., Kashinath, K., et al. (2025). *FourCastNet 3: A geometric approach to probabilistic machine-learning weather forecasting at scale*. arXiv [cs.LG].

Brenowitz, N. D., Beucler, T., Pritchard, M., & Bretherton, C. S. (2020). Interpreting and stabilizing Machine-Learning parametrizations of convection. *Journal of the Atmospheric Sciences*, *77*(12), 4357–4375. https://doi.org/10.1175/jas-d-20-0082.1

Brenowitz, N. D., & Bretherton, C. S. (2019). Spatially extended tests of a neural network parametrization trained by coarse-graining. *Journal of Advances in Modeling Earth Systems*, *11*(8), 2728–2744. https://doi.org/10.1029/2019ms001711

Ceppi, P., & Hartmann, D. L. (2016). Clouds and the atmospheric circulation response to warming. *Journal of Climate*, *29*(2), 783–799. https://doi.org/10.1175/jcli-d-15-0394.1

Chen, J., Zhang, M., Zhang, T., Lin, W., & Xue, W. (2025). Stable simulation of the community atmosphere model using machine-learning physical parameterization trained with experience replay. *Journal of Advances in Modeling Earth Systems*, *17*(6), e2024MS004722. https://doi.org/10.1029/2024ms004722

Chow, A., Cameron, G., Georg, M., Sherwood, M., Culliton, P., Sepah, S., et al. (2023). *Google - American sign language fingerspelling recognition*. Kaggle. Retrieved from https://kaggle.com/competitions/asl-fingerspelling

Christensen, H. M., Barker, J., Antonio, B., Bonavita, M., Dahoui, M., & de Rosnay, P. (2026). *Error in ERA5 2m temperature identified using GraphCast*. arXiv [physics.ao-ph].

Christensen, H. M., Kouhen, S., Miller, G., & Parthipan, R. (2024). Machine learning for stochastic parametrization. *Environ. Data Science*, *3*(e38), e38. https://doi.org/10.1017/eds.2024.45

19422466, 2026, 5, Downloaded from https://agupubs.onlinelibrary.wiley.com/doi/10.1029/2025MS005643 by Dtsch Zentrum F. Luft-U. Raum Fahrt In D. Helmholtz Gemein., Wiley Online Library on [27/10/2026]. See the Terms and Conditions (https://onlinelibrary.wiley.com/terms-and-conditions) on Wiley Online Library for rules of use; OA articles are governed by the applicable Creative Commons License

Clark, S. K., Brenowitz, N. D., Henn, B., Kwa, A., McGibbon, J., Perkins, W. A., et al. (2022). Correcting a 200 km resolution climate model in multiple climates by machine learning from 25 km resolution simulations. *Journal of Advances in Modeling Earth Systems*, *14*(9), e2022MS003219. https://doi.org/10.1029/2022ms003219

Colin, M., Sherwood, S., Geoffroy, O., Bony, S., & Fuchs, D. (2019). Identifying the sources of convective memory in Cloud-Resolving simulations. *Journal of the Atmospheric Sciences*, *76*(3), 947–962. https://doi.org/10.1175/jas-d-18-0036.1

Das, R., He, S., Huang, R., Townley, J., Kretsch, R., Karagianes, T., et al. (2023). *Stanford ribonanza rna folding*. Kaggle. Retrieved from https://kaggle.com/competitions/stanford-ribonanza-rna-folding

Davenport, E. H., Madan, J. V., Gjini, R., Brzenski, J., Ho, N., Hsu, T.-Y., et al. (2026). JCM v1.0: A differentiable, intermediate-complexity atmospheric model. *EGUsphere*, 1–20.

Dheeshjith, S., Subel, A., Adcroft, A., Busecke, J., Fernandez-Granda, C., Gupta, S., & Zanna, L. (2025). Samudra: An AI global ocean emulator for climate. *Geophysical Research Letters*, *52*(10), e2024GL114318. https://doi.org/10.1029/2024gl114318

Dheeshjith, S., Subel, A., Gupta, S., Adcroft, A., Fernandez-Granda, C., Busecke, J., & Zanna, L. (2024). *Transfer learning for emulating ocean climate variability across CO_2 forcing*. arXiv [physics.ao-ph].

Duncan, J. P. C., Wu, E., Dheeshjith, S., Subel, A., Arcomano, T., Clark, S. K., et al. (2025). *SamudrACE: Fast and accurate coupled climate modeling with 3D ocean and atmosphere emulators*. arXiv [physics.ao-ph].

Gentine, P., Pritchard, M., Rasp, S., Reinaudi, G., & Yacalis, G. (2018). Could machine learning break the convection parameterization deadlock? *Geophysical Research Letters*, *45*(11), 5742–5751. https://doi.org/10.1029/2018gl078202

Grinsztajn, L., Oyallon, E., & Varoquaux, G. (2022). Why do tree-based models still outperform deep learning on typical tabular data? In *Proceedings of the 36th international conference on neural information processing systems* (pp. 507–520). Curran Associates Inc.

Han, Y., Zhang, G. J., & Wang, Y. (2023). An ensemble of neural networks for moist physics processes, its generalizability and stable integration. *Journal of Advances in Modeling Earth Systems*, *15*(10), e2022MS003508. https://doi.org/10.1029/2022ms003508

Han, Y., Zhang, G. J., Wang, Y., & Wan, H. (2025). A decadal hybrid GCM simulation using deep-learning-based cloud and convection parameterization generalized to a warm climate. *Journal of Advances in Modeling Earth Systems*, *17*(12), e2025MS005231. https://doi.org/10.1029/2025ms005231

Hannah, W., & Pressel, K. (2022). A method for transporting cloud-resolving model variance in a multiscale modeling framework. *Geoscientific Model Development*, *15*(24), 8999–9013. https://doi.org/10.5194/gmd-15-8999-2022

Hannah, W. M., Jones, C. R., Hillman, B. R., Norman, M. R., Bader, D. C., Taylor, M. A., et al. (2020). Initial results from the super-parameterized E3SM. *Journal of Advances in Modeling Earth Systems*, *12*(1), e2019MS001863. https://doi.org/10.1029/2019ms001863

Hannah, W. M., Mahajan, S., Harrop, B. E., Liu, N., Peng, L., Pritchard, M. S., et al. (2025). Coupled climate simulations with E3SM-MMF. *Journal of Advances in Modeling Earth Systems*, *17*(9), e2025MS004935. https://doi.org/10.1029/2025ms004935

Heuer, H., Beucler, T., Schwabe, M., Savre, J., Schlund, M., & Eyring, V. (2025). *Beyond the training data: Confidence-guided mixing of parameterizations in a hybrid AI-climate model*. arXiv [physics.ao-ph].

Heuer, H., Schwabe, M., Gentine, P., Giorgetta, M. A., & Eyring, V. (2024). Interpretable multiscale machine learning-based parameterizations of convection for ICON. *Journal of Advances in Modeling Earth Systems*, *16*(8), e2024MS004398. https://doi.org/10.1029/2024ms004398

Hohenegger, C., Korn, P., Linardakis, L., Redler, R., Schnur, R., Adamidis, P., et al. (2023). ICON-sapphire: Simulating the components of the earth system and their interactions at kilometer and subkilometer scales. *Geoscientific Model Development*, *16*(2), 779–811. https://doi.org/10.5194/gmd-16-779-2023

Hu, Z., Subramaniam, A., Kuang, Z., Lin, J., Yu, S., Hannah, W. M., et al. (2025). Stable machine-learning parameterization of subgrid processes in a comprehensive atmospheric model learned from embedded convection-permitting simulations. *Journal of Advances in Modeling Earth Systems*, *17*(7), e2024MS004618. https://doi.org/10.1029/2024ms004618

Hwong, Y.-L., Colin, M., Aglas-Leitner, P., Muller, C. J., & Sherwood, S. C. (2023). Assessing memory in convection schemes using idealized tests. *Journal of Advances in Modeling Earth Systems*, *15*(12), e2023MS003726. https://doi.org/10.1029/2023ms003726

Iglesias-Suarez, F., Gentine, P., Solino-Fernandez, B., Beucler, T., Pritchard, M., Runge, J., & Eyring, V. (2024). Causally-informed deep learning to improve climate models and projections. *Journal of Geophysical Research: Atmospheres*, *129*(4), e2023JD039202. https://doi.org/10.1029/2023jd039202

Jansson, F., van den Oord, G., Pelupessy, I., Chertova, M., Grönqvist, J. H., Siebesma, A. P., & Crommelin, D. (2022). Representing cloud mesoscale variability in superparameterized climate models. *Journal of Advances in Modeling Earth Systems*, *14*(8), e2021MS002892. https://doi.org/10.1029/2021ms002892

Januschowski, T., Wang, Y., Torkkola, K., Erkkilä, T., Hasson, H., & Gasthaus, J. (2022). Forecasting with trees. *International Journal of Forecasting*, *38*(4), 1473–1481. https://doi.org/10.1016/j.ijforecast.2021.10.004

Karlbauer, M., Cresswell-Clay, N., Durran, D. R., Moreno, R. A., Kurth, T., Bonev, B., et al. (2024). Advancing parsimonious deep learning weather prediction using the HEALPix mesh. *Journal of Advances in Modeling Earth Systems*, *16*(8), e2023MS004021. https://doi.org/10.1029/2023ms004021

Kay, J. E., Deser, C., Phillips, A., Mai, A., Hannay, C., Strand, G., et al. (2015). The community earth system model (CESM) large ensemble project: A community resource for studying climate change in the presence of internal climate variability. *Bulletin of the American Meteorological Society*, *96*(8), 1333–1349. https://doi.org/10.1175/bams-d-13-00255.1

Khairoutdinov, M., Randall, D., & DeMott, C. (2005). Simulations of the atmospheric general circulation using a cloud-resolving model as a superparameterization of physical processes. *Journal of the Atmospheric Sciences*, *62*(7), 2136–2154. https://doi.org/10.1175/jas3453.1

Kim, S., Gholami, A., Shaw, A., Lee, N., Mangalam, K., Malik, J., & Keutzer, K. (2022). *Squeezeformer: An efficient transformer for automatic speech recognition*. arxiv:2206.00888.

Kochkov, D., Yuval, J., Langmore, I., Norgaard, P., Smith, J., Mooers, G., et al. (2024). Neural general circulation models for weather and climate. *Nature*, *632*, 1060–1066. https://doi.org/10.1038/s41586-024-07744-y

Koehler, F., & Thuerey, N. (2025). Neural emulator superiority: When machine learning for PDEs surpasses its training data. In *The thirty-ninth annual conference on neural information processing systems*.

Leutbecher, M., Lock, S.-J., Ollinaho, P., Lang, S. T. K., Balsamo, G., Bechtold, P., et al. (2017). Stochastic representations of model uncertainties at ECMWF: State of the art and future vision: Stochastic representations of model uncertainties. *Quarterly Journal of the Royal Meteorological Society*, *143*(707), 2315–2339. https://doi.org/10.1002/qj.3094

Li, F., Rosa, D., Collins, W. D., & Wehner, M. F. (2012). "super-parameterization": A better way to simulate regional extreme precipitation? *Journal of Advances in Modeling Earth Systems*, *4*(2). https://doi.org/10.1029/2011ms000106

Lin, J., Hu, Z., Yu, S., Pritchard, M., Gupta, R., Zheng, T., et al. (2024). *Leap—Atmospheric physics using AI (ClimSim)*. Kaggle. Retrieved from https://kaggle.com/competitions/leap-atmospheric-physics-ai-climsim

19422466, 2026, 5, Downloaded from https://agupubs.onlinelibrary.wiley.com/doi/10.1029/2025MS005643 by Dtsch Zentrum F. Luft-U. Raum Fahrt In D. Helmholtz Gemein., Wiley Online Library on [27/10/2026]. See the Terms and Conditions (https://onlinelibrary.wiley.com/terms-and-conditions) on Wiley Online Library for rules of use; OA articles are governed by the applicable Creative Commons License

Lin, J., Yu, S., Peng, L., Beucler, T., Wong-Toi, E., Hu, Z., et al. (2025). Navigating the noise: Bringing clarity to ML parameterization design with O(100) ensembles. *Journal of Advances in Modeling Earth Systems*, *17*(4), e2024MS004551. https://doi.org/10.1029/2024ms004551

Liu, S., & O'Gorman, P. A. (2025). *CERA: A framework for improved generalization of machine learning models to changed climates*. arXiv [physics.ao-ph].

Liu, Z., Mao, H., Wu, C.-Y., Feichtenhofer, C., Darrell, T., & Xie, S. (2022). A convnet for the 2020s. In *Proceedings of the IEEE/CVF conference on computer vision and pattern recognition (CVPR)*.

Mansfield, L. A., Gupta, A., Burnett, A. C., Green, B., Wilka, C., & Sheshadri, A. (2023). Updates on model hierarchies for understanding and simulating the climate system: A focus on data-informed methods and climate change impacts. *Journal of Advances in Modeling Earth Systems*, *15*(10), e2023MS003715. https://doi.org/10.1029/2023ms003715

Medeiros, B., Clement, A. C., Benedict, J. J., & Zhang, B. (2021). Investigating the impact of cloud-radiative feedbacks on tropical precipitation extremes. *npj Climate and Atmospheric Science*, *4*(1), 1–10. https://doi.org/10.1038/s41612-021-00174-x

Mooers, G., Pritchard, M., Beucler, T., Ott, J., Yacalis, G., Baldi, P., & Gentine, P. (2021). Assessing the potential of deep learning for emulating cloud superparameterization in climate models with real-geography boundary conditions. *Journal of Advances in Modeling Earth Systems*, *13*(5), e2020MS002385. https://doi.org/10.1029/2020ms002385

O'Gorman, P. A. (2012). Sensitivity of tropical precipitation extremes to climate change. *Nature Geoscience*, *5*(10), 697–700. https://doi.org/10.1038/ngeo1568

Pincus, R., Iacono, M. J., Alexeev, D., Adamidis, P., Hillman, B. R., Norman, M., et al. (2023). RTE+RRTMGP. Retrieved from https://github.com/earth-system-radiaton/rte-rrtmgp

Pincus, R., Mlawer, E. J., & Delamere, J. S. (2019). Balancing accuracy, efficiency, and flexibility in radiation calculations for dynamical models. *Journal of Advances in Modeling Earth Systems*, *11*(10), 3074–3089. https://doi.org/10.1029/2019ms001621

Pritchard, M. S., Moncrieff, M. W., & Somerville, R. C. J. (2011). Orogenic propagating precipitation systems over the United States in a global climate model with embedded explicit convection. *Journal of the Atmospheric Sciences*, *68*(8), 1821–1840. https://doi.org/10.1175/2011jas3699.1

Randall, D. (2013). Beyond deadlock. *Geophysical Research Letters*, *40*(22), 5970–5976. https://doi.org/10.1002/2013gl057998

Randall, D., Khairoutdinov, M., Arakawa, A., & Grabowski, W. (2003). Breaking the cloud parameterization deadlock. *Bulletin of the American Meteorological Society*, *84*(11), 1547–1564. https://doi.org/10.1175/bams-84-11-1547

Rasp, S., Pritchard, M., & Gentine, P. (2018). Deep learning to represent subgrid processes in climate models.

Schneider, T., Leung, L. R., & Wills, R. C. J. (2024). Opinion: Optimizing climate models with process knowledge, resolution, and artificial intelligence. *Atmospheric Chemistry and Physics*, *24*(12), 7041–7062. https://doi.org/10.5194/acp-24-7041-2024

Schneider, T., Teixeira, J., Bretherton, C. S., Brient, F., Pressel, K. G., Schär, C., & Pier Siebesma, A. (2017). Climate goals and computing the future of clouds. *Nature Climate Change*, *7*(1), 3–5. https://doi.org/10.1038/nclimate3190

Shamekh, S., Lamb, K. D., Huang, Y., & Gentine, P. (2023). Implicit learning of convective organization explains precipitation stochasticity. *Proceedings of the National Academy of Sciences*, *120*(20), e2216158120. https://doi.org/10.1073/pnas.2216158120

Sherwood, S. C., Bony, S., & Dufresne, J.-L. (2014). Spread in model climate sensitivity traced to atmospheric convective mixing. *Nature*, *505*(7481), 37–42. https://doi.org/10.1038/nature12829

Song, Y., Sohl-Dickstein, J., Kingma, D. P., Kumar, A., Ermon, S., & Poole, B. (2020). *Score-based generative modeling through stochastic differential equations*. arXiv preprint arXiv:2011.13456.

Stan, C., Khairoutdinov, M., DeMott, C. A., Krishnamurthy, V., Straus, D. M., Randall, D. A., et al. (2010). An ocean-atmosphere climate simulation with an embedded cloud resolving model: A global climate simulation. *Geophysical Research Letters*, *37*(1), L01702. https://doi.org/10.1029/2009GL040822

Taylor, M., Caldwell, P. M., Bertagna, L., Clevenger, C., Donahue, A., Foucar, J., et al. (2023). The simple cloud-resolving E3SM atmosphere model running on the Frontier exascale system. In *Proceedings of the international conference for high performance computing, networking, storage and analysis* (pp. 1–11). Association for Computing Machinery.

Ukkonen, P., & Chantry, M. (2025). Vertically recurrent neural networks for sub-grid parameterization. *Journal of Advances in Modeling Earth Systems*, *17*(6), e2024MS004833. https://doi.org/10.1029/2024ms004833

Wang, X., Han, Y., Xue, W., Yang, G., & Zhang, G. J. (2022). Stable climate simulations using a realistic general circulation model with neural network parameterizations for atmospheric moist physics and radiation processes. *Geoscientific Model Development*, *15*(9), 3923–3940. https://doi.org/10.5194/gmd-15-3923-2022

Webb, M. J., Lambert, F. H., & Gregory, J. M. (2013). Origins of differences in climate sensitivity, forcing and feedback in climate models. *Climate Dynamics*, *40*(3–4), 677–707. https://doi.org/10.1007/s00382-012-1336-x

Xia, Y., Lin, Y.-F., Yu, J.-Y., Hannah, W., & Pritchard, M. (2025). *Diagnosing biases in tropical Atlantic-Pacific multi-decadal teleconnections across CMIP6 and E3SM models*. arXiv [physics.ao-ph].

Yu, S., Hannah, W., Peng, L., Lin, J., Bhouri, M. A., Gupta, R., et al. (2023). ClimSim: A large multi-scale dataset for hybrid physics-ML climate emulation.

Yu, S., Hu, Z., Subramaniam, A., Hannah, W., Peng, L., Lin, J., et al. (2025). ClimSim-online: A large multi-scale dataset and framework for hybrid physics-ML climate emulation. *Journal of Machine Learning Research*, *26*(142), 1–85.

Yuval, J., Langmore, I., Kochkov, D., & Hoyer, S. (2026). Neural general circulation models for modeling precipitation. *Science Advances*, *12*(2), eadv6891. https://doi.org/10.1126/sciadv.adv6891

19422466, 2026, 5, Downloaded from https://agupubs.onlinelibrary.wiley.com/doi/10.1029/2025MS005643 by Dtsch Zentrum F. Luft-U. Raum Fahrt In D. Helmholtz Gemein., Wiley Online Library on [27/10/2026]. See the Terms and Conditions (https://onlinelibrary.wiley.com/terms-and-conditions) on Wiley Online Library for rules of use; OA articles are governed by the applicable Creative Commons License